Measurement of sin^{2}θ_{eff}^{lept} using e^{+}e^{-} pairs from γ^{*}/Z bosons produced in pp[over ¯] collisions at a center-of-momentum energy of 1.96 TeV

T. Aaltonen *et al.* (CDF Collaboration)

Phys. Rev. D **93**, 112016 — Published 28 June 2016

DOI: 10.1103/PhysRevD.93.112016

Measurement of $\sin^2\theta^{\rm lept}_{\rm eff}$ using e^+e^- pairs from γ^*/Z bosons produced in $p\bar{p}$ collisions at a center-of-momentum energy of 1.96 TeV

T. Aaltonen,[21] S. Amerio[ll],[39] D. Amidei,[31] A. Anastassov[w],[15] A. Annovi,[17] J. Antos,[12] G. Apollinari,[15] J.A. Appel,[15] T. Arisawa,[51] A. Artikov,[13] J. Asaadi,[47] W. Ashmanskas,[15] B. Auerbach,[2] A. Aurisano,[47] F. Azfar,[38] W. Badgett,[15] T. Bae,[25] A. Barbaro-Galtieri,[26] V.E. Barnes,[43] B.A. Barnett,[23] P. Barria[nn],[41] P. Bartos,[12] M. Bauce[ll],[39] F. Bedeschi,[41] S. Behari,[15] G. Bellettini[mm],[41] J. Bellinger,[53] D. Benjamin,[14] A. Beretvas,[15] A. Bhatti,[45] K.R. Bland,[5] B. Blumenfeld,[23] A. Bocci,[14] A. Bodek,[44] D. Bortoletto,[43] J. Boudreau,[42] A. Boveia,[11] L. Brigliadori[kk],[6] C. Bromberg,[32] E. Brucken,[21] J. Budagov,[13] H.S. Budd,[44] K. Burkett,[15] G. Busetto[ll],[39] P. Bussey,[19] P. Butti[mm],[41] A. Buzatu,[19] A. Calamba,[10] S. Camarda,[4] M. Campanelli,[28] F. Canelli[ee],[11] B. Carls,[22] D. Carlsmith,[53] R. Carosi,[41] S. Carrillo[l],[16] B. Casal[j],[9] M. Casarsa,[48] A. Castro[kk],[6] P. Catastini,[20] D. Cauz[ss,tt],[48] V. Cavaliere,[22] A. Cerri[e],[26] L. Cerrito[r],[28] Y.C. Chen,[1] M. Chertok,[7] G. Chiarelli,[41] G. Chlachidze,[15] K. Cho,[25] D. Chokheli,[13] A. Clark,[18] C. Clarke,[52] M.E. Convery,[15] J. Conway,[7] M. Corbo[z],[15] M. Cordelli,[17] C.A. Cox,[7] D.J. Cox,[7] M. Cremonesi,[41] D. Cruz,[47] J. Cuevas[y],[9] R. Culbertson,[15] N. d'Ascenzo[v],[15] M. Datta[hh],[15] P. de Barbaro,[44] L. Demortier,[45] M. Deninno,[6] M. D'Errico[ll],[39] F. Devoto,[21] A. Di Canto[mm],[41] B. Di Ruzza[p],[15] J.R. Dittmann,[5] S. Donati[mm],[41] M. D'Onofrio,[27] M. Dorigo[uu],[48] A. Driutti[ss,tt],[48] K. Ebina,[51] R. Edgar,[31] R. Erbacher,[7] S. Errede,[22] B. Esham,[22] S. Farrington,[38] J.P. Fernández Ramos,[29] R. Field,[16] G. Flanagan[t],[15] R. Forrest,[7] M. Franklin,[20] J.C. Freeman,[15] H. Frisch,[11] Y. Funakoshi,[51] C. Galloni[mm],[41] A.F. Garfinkel,[43] P. Garosi[nn],[41] H. Gerberich,[22] E. Gerchtein,[15] S. Giagu,[46] V. Giakoumopoulou,[3] K. Gibson,[42] C.M. Ginsburg,[15] N. Giokaris,[3] P. Giromini,[17] V. Glagolev,[13] D. Glenzinski,[15] M. Gold,[34] D. Goldin,[47] A. Golossanov,[15] G. Gomez,[9] G. Gomez-Ceballos,[30] M. Goncharov,[30] O. González López,[29] I. Gorelov,[34] A.T. Goshaw,[14] K. Goulianos,[45] E. Gramellini,[6] C. Grosso-Pilcher,[11] J. Guimaraes da Costa,[20] S.R. Hahn,[15] J.Y. Han,[44] F. Happacher,[17] K. Hara,[49] M. Hare,[50] R.F. Harr,[52] T. Harrington-Taber[m],[15] K. Hatakeyama,[5] C. Hays,[38] J. Heinrich,[40] M. Herndon,[53] A. Hocker,[15] Z. Hong,[47] W. Hopkins[f],[15] S. Hou,[1] R.E. Hughes,[35] U. Husemann,[54] M. Hussein[cc],[32] J. Huston,[32] G. Introzzi[pp,qq],[41] M. Iori[rr],[46] A. Ivanov[o],[7] E. James,[15] D. Jang,[10] B. Jayatilaka,[15] E.J. Jeon,[25] S. Jindariani,[15] M. Jones,[43] K.K. Joo,[25] S.Y. Jun,[10] T.R. Junk,[15] M. Kambeitz,[24] T. Kamon,[25,47] P.E. Karchin,[52] A. Kasmi,[5] Y. Kato[n],[37] W. Ketchum[ii],[11] J. Keung,[40] B. Kilminster[ee],[15] D.H. Kim,[25] H.S. Kim[bb],[15] J.E. Kim,[25] M.J. Kim,[17] S.H. Kim,[49] S.B. Kim,[25] Y.J. Kim,[25] Y.K. Kim,[11] N. Kimura,[51] M. Kirby,[15] K. Kondo,[51,*] D.J. Kong,[25] J. Konigsberg,[16] A.V. Kotwal,[14] M. Kreps,[24] J. Kroll,[40] M. Kruse,[14] T. Kuhr,[24] M. Kurata,[49] A.T. Laasanen,[43] S. Lammel,[15] M. Lancaster,[28] K. Lannon[x],[35] G. Latino[nn],[41] H.S. Lee,[25] J.S. Lee,[25] S. Leo,[22] S. Leone,[41] J.D. Lewis,[15] A. Limosani[s],[14] E. Lipeles,[40] A. Lister[a],[18] Q. Liu,[43] T. Liu,[15] S. Lockwitz,[54] A. Loginov,[54,*] D. Lucchesi[ll],[39] A. Lucà,[17] J. Lueck,[24] P. Lujan,[26] P. Lukens,[15] G. Lungu,[45] J. Lys,[26] R. Lysak[d],[12] R. Madrak,[15] P. Maestro[nn],[41] S. Malik,[45] G. Manca[b],[27] A. Manousakis-Katsikakis,[3] L. Marchese[jj],[6] F. Margaroli,[46] P. Marino[oo],[41] K. Matera,[22] M.E. Mattson,[52] A. Mazzacane,[15] P. Mazzanti,[6] R. McNulty[i],[27] A. Mehta,[27] P. Mehtala,[21] C. Mesropian,[45] T. Miao,[15] D. Mietlicki,[31] A. Mitra,[1] H. Miyake,[49] S. Moed,[15] N. Moggi,[6] C.S. Moon[z],[15] R. Moore[ff,gg],[15] M.J. Morello[oo],[41] A. Mukherjee,[15] Th. Muller,[24] P. Murat,[15] M. Mussini[kk],[6] J. Nachtman[m],[15] Y. Nagai,[49] J. Naganoma,[51] I. Nakano,[36] A. Napier,[50] J. Nett,[47] T. Nigmanov,[42] L. Nodulman,[2] S.Y. Noh,[25] O. Norniella,[22] L. Oakes,[38] S.H. Oh,[14] Y.D. Oh,[25] T. Okusawa,[37] R. Orava,[21] L. Ortolan,[4] C. Pagliarone,[48] E. Palencia[e],[9] P. Palni,[34] V. Papadimitriou,[15] W. Parker,[53] G. Pauletta[ss,tt],[48] M. Paulini,[10] C. Paus,[30] T.J. Phillips,[14] G. Piacentino[q],[15] E. Pianori,[40] J. Pilot,[7] K. Pitts,[22] C. Plager,[8] L. Pondrom,[53] S. Poprocki[f],[15] K. Potamianos,[26] A. Pranko,[26] F. Prokoshin[aa],[13] F. Ptohos[g],[17] G. Punzi[mm],[41] I. Redondo Fernández,[29] P. Renton,[38] M. Rescigno,[46] F. Rimondi,[6,*] L. Ristori,[41,15] A. Robson,[19] T. Rodriguez,[40] S. Rolli[h],[50] M. Ronzani[mm],[41] R. Roser,[15] J.L. Rosner,[11] F. Ruffini[nn],[41] A. Ruiz,[9] J. Russ,[10] V. Rusu,[15] W.K. Sakumoto,[44] Y. Sakurai,[51] L. Santi[ss,tt],[48] K. Sato,[49] V. Saveliev[v],[15] A. Savoy-Navarro[z],[15] P. Schlabach,[15] E.E. Schmidt,[15] T. Schwarz,[31] L. Scodellaro,[9] F. Scuri,[41] S. Seidel,[34] Y. Seiya,[37] A. Semenov,[13] F. Sforza[mm],[41] S.Z. Shalhout,[7] T. Shears,[27] P.F. Shepard,[42] M. Shimojima[u],[49] M. Shochet,[11] I. Shreyber-Tecker,[33] A. Simonenko,[13] K. Sliwa,[50] J.R. Smith,[7] F.D. Snider,[15] H. Song,[42] V. Sorin,[4] R. St. Denis,[19,*] M. Stancari,[15] D. Stentz[w],[15] J. Strologas,[34] Y. Sudo,[49] A. Sukhanov,[15] I. Suslov,[13] K. Takemasa,[49] Y. Takeuchi,[49] J. Tang,[11] M. Tecchio,[31] P.K. Teng,[1] J. Thom[f],[15] E. Thomson,[40] V. Thukral,[47] D. Toback,[47] S. Tokar,[12] K. Tollefson,[32] T. Tomura,[49] D. Tonelli[e],[15] S. Torre,[17] D. Torretta,[15] P. Totaro,[39] M. Trovato[oo],[41] F. Ukegawa,[49] S. Uozumi,[25] F. Vázquez[l],[16] G. Velev,[15] C. Vellidis,[15] C. Vernieri[oo],[41] M. Vidal,[43] R. Vilar,[9] J. Vizán[dd],[9] M. Vogel,[34] G. Volpi,[17] P. Wagner,[40] R. Wallny[j],[15]

S.M. Wang,[1] D. Waters,[28] W.C. Wester III,[15] D. Whiteson[c],[40] A.B. Wicklund,[2] S. Wilbur,[7] H.H. Williams,[40] J.S. Wilson,[31] P. Wilson,[15] B.L. Winer,[35] P. Wittich[f],[15] S. Wolbers,[15] H. Wolfe,[35] T. Wright,[31] X. Wu,[18] Z. Wu,[5] K. Yamamoto,[37] D. Yamato,[37] T. Yang,[15] U.K. Yang,[25] Y.C. Yang,[25] W.-M. Yao,[26] G.P. Yeh,[15] K. Yi[m],[15] J. Yoh,[15] K. Yorita,[51] T. Yoshida[k],[37] G.B. Yu,[14] I. Yu,[25] A.M. Zanetti,[48] Y. Zeng,[14] C. Zhou,[14] and S. Zucchelli[kk6]

(CDF Collaboration)[†]

[1] *Institute of Physics, Academia Sinica, Taipei, Taiwan 11529, Republic of China*
[2] *Argonne National Laboratory, Argonne, Illinois 60439, USA*
[3] *University of Athens, 157 71 Athens, Greece*
[4] *Institut de Fisica d'Altes Energies, ICREA, Universitat Autonoma de Barcelona, E-08193, Bellaterra (Barcelona), Spain*
[5] *Baylor University, Waco, Texas 76798, USA*
[6] *Istituto Nazionale di Fisica Nucleare Bologna, [kk] University of Bologna, I-40127 Bologna, Italy*
[7] *University of California, Davis, Davis, California 95616, USA*
[8] *University of California, Los Angeles, Los Angeles, California 90024, USA*
[9] *Instituto de Fisica de Cantabria, CSIC-University of Cantabria, 39005 Santander, Spain*
[10] *Carnegie Mellon University, Pittsburgh, Pennsylvania 15213, USA*
[11] *Enrico Fermi Institute, University of Chicago, Chicago, Illinois 60637, USA*
[12] *Comenius University, 842 48 Bratislava, Slovakia; Institute of Experimental Physics, 040 01 Kosice, Slovakia*
[13] *Joint Institute for Nuclear Research, RU-141980 Dubna, Russia*
[14] *Duke University, Durham, North Carolina 27708, USA*
[15] *Fermi National Accelerator Laboratory, Batavia, Illinois 60510, USA*
[16] *University of Florida, Gainesville, Florida 32611, USA*
[17] *Laboratori Nazionali di Frascati, Istituto Nazionale di Fisica Nucleare, I-00044 Frascati, Italy*
[18] *University of Geneva, CH-1211 Geneva 4, Switzerland*
[19] *Glasgow University, Glasgow G12 8QQ, United Kingdom*
[20] *Harvard University, Cambridge, Massachusetts 02138, USA*
[21] *Division of High Energy Physics, Department of Physics, University of Helsinki, FIN-00014, Helsinki, Finland; Helsinki Institute of Physics, FIN-00014, Helsinki, Finland*
[22] *University of Illinois, Urbana, Illinois 61801, USA*
[23] *The Johns Hopkins University, Baltimore, Maryland 21218, USA*
[24] *Institut für Experimentelle Kernphysik, Karlsruhe Institute of Technology, D-76131 Karlsruhe, Germany*
[25] *Center for High Energy Physics: Kyungpook National University, Daegu 702-701, Korea; Seoul National University, Seoul 151-742, Korea; Sungkyunkwan University, Suwon 440-746, Korea; Korea Institute of Science and Technology Information, Daejeon 305-806, Korea; Chonnam National University, Gwangju 500-757, Korea; Chonbuk National University, Jeonju 561-756, Korea; Ewha Womans University, Seoul, 120-750, Korea*
[26] *Ernest Orlando Lawrence Berkeley National Laboratory, Berkeley, California 94720, USA*
[27] *University of Liverpool, Liverpool L69 7ZE, United Kingdom*
[28] *University College London, London WC1E 6BT, United Kingdom*
[29] *Centro de Investigaciones Energeticas Medioambientales y Tecnologicas, E-28040 Madrid, Spain*
[30] *Massachusetts Institute of Technology, Cambridge, Massachusetts 02139, USA*
[31] *University of Michigan, Ann Arbor, Michigan 48109, USA*
[32] *Michigan State University, East Lansing, Michigan 48824, USA*
[33] *Institution for Theoretical and Experimental Physics, ITEP, Moscow 117259, Russia*
[34] *University of New Mexico, Albuquerque, New Mexico 87131, USA*
[35] *The Ohio State University, Columbus, Ohio 43210, USA*
[36] *Okayama University, Okayama 700-8530, Japan*
[37] *Osaka City University, Osaka 558-8585, Japan*
[38] *University of Oxford, Oxford OX1 3RH, United Kingdom*
[39] *Istituto Nazionale di Fisica Nucleare, Sezione di Padova, [ll] University of Padova, I-35131 Padova, Italy*
[40] *University of Pennsylvania, Philadelphia, Pennsylvania 19104, USA*
[41] *Istituto Nazionale di Fisica Nucleare Pisa, [mm] University of Pisa, [nn] University of Siena, [oo] Scuola Normale Superiore, I-56127 Pisa, Italy, [pp] INFN Pavia, I-27100 Pavia, Italy, [qq] University of Pavia, I-27100 Pavia, Italy*
[42] *University of Pittsburgh, Pittsburgh, Pennsylvania 15260, USA*
[43] *Purdue University, West Lafayette, Indiana 47907, USA*
[44] *University of Rochester, Rochester, New York 14627, USA*
[45] *The Rockefeller University, New York, New York 10065, USA*
[46] *Istituto Nazionale di Fisica Nucleare, Sezione di Roma 1, [rr] Sapienza Università di Roma, I-00185 Roma, Italy*

[47] Mitchell Institute for Fundamental Physics and Astronomy, Texas A&M University, College Station, Texas 77843, USA
[48] Istituto Nazionale di Fisica Nucleare Trieste, [ss] Gruppo Collegato di Udine, [tt] University of Udine, I-33100 Udine, Italy, [uu] University of Trieste, I-34127 Trieste, Italy
[49] University of Tsukuba, Tsukuba, Ibaraki 305, Japan
[50] Tufts University, Medford, Massachusetts 02155, USA
[51] Waseda University, Tokyo 169, Japan
[52] Wayne State University, Detroit, Michigan 48201, USA
[53] University of Wisconsin-Madison, Madison, Wisconsin 53706, USA
[54] Yale University, New Haven, Connecticut 06520, USA

(Dated: June 8, 2016)

At the Fermilab Tevatron proton-antiproton ($p\bar{p}$) collider, Drell-Yan lepton pairs are produced in the process $p\bar{p} \to e^+e^- + X$ through an intermediate γ^*/Z boson. The forward-backward asymmetry in the polar-angle distribution of the e^- as a function of the e^+e^--pair mass is used to obtain $\sin^2\theta^{\rm lept}_{\rm eff}$, the effective leptonic determination of the electroweak-mixing parameter $\sin^2\theta_W$. The measurement sample, recorded by the Collider Detector at Fermilab (CDF), corresponds to 9.4 fb^{-1} of integrated luminosity from $p\bar{p}$ collisions at a center-of-momentum energy of 1.96 TeV, and is the full CDF Run II data set. The value of $\sin^2\theta^{\rm lept}_{\rm eff}$ is found to be 0.23248 ± 0.00053. The combination with the previous CDF measurement based on $\mu^+\mu^-$ pairs yields $\sin^2\theta^{\rm lept}_{\rm eff} = 0.23221 \pm 0.00046$. This result, when interpreted within the specified context of the standard model assuming $\sin^2\theta_W = 1 - M_W^2/M_Z^2$ and that the W- and Z-boson masses are on-shell, yields $\sin^2\theta_W = 0.22400 \pm 0.00045$, or equivalently a W-boson mass of 80.328 ± 0.024 GeV/c^2.

PACS numbers: 12.15.Lk, 13.85.Qk, 14.70.Hp

I. INTRODUCTION

In this paper, the angular distribution of charged leptons ($\ell^\pm$) from the Drell-Yan [1] process is used to measure the electroweak-mixing parameter $\sin^2\theta_W$ [2]. At the Fermilab Tevatron collider, Drell-Yan pairs are produced by the process $p\bar{p} \to \ell^+\ell^- + X$, where the $\ell^+\ell^-$ pair is produced through an intermediate γ^*/Z boson, and X is the final state associated with the production of the boson. In the standard model, the production of Drell-Yan lepton pairs at the Born level proceeds through two parton-level processes,

$$q\bar{q} \to \gamma^* \to \ell^+\ell^- \text{ and}$$
$$q\bar{q} \to Z \to \ell^+\ell^-,$$

where the q and $\bar{q}$ are the quark and antiquark, respectively, from the colliding hadrons. The virtual photon couples the vector currents of the incoming and outgoing fermions (f), and the spacetime structure of a photon-fermion interaction vertex is $\langle \bar{f}|Q_f\gamma_\mu|f\rangle$, where Q_f, the strength of the coupling, is the fermion charge (in units of e), and $|f\rangle$ is the spinor for fermion f. An interaction vertex of a fermion with a Z boson contains both vector (V) and axial-vector (A) current components, and its structure is $\langle \bar{f}|g_V^f\gamma_\mu + g_A^f\gamma_\mu\gamma_5|f\rangle$. The Born-level coupling strengths are

$$g_V^f = T_3^f - 2Q_f \sin^2\theta_W \text{ and}$$
$$g_A^f = T_3^f,$$

where T_3^f is the third component of the fermion weak-isospin, which is $T_3^f = \frac{1}{2}$ $(-\frac{1}{2})$ for positively (negatively) charged fermions. At the Born level, and in all

---

* Deceased

† With visitors from [a] University of British Columbia, Vancouver, BC V6T 1Z1, Canada, [b] Istituto Nazionale di Fisica Nucleare, Sezione di Cagliari, 09042 Monserrato (Cagliari), Italy, [c] University of California Irvine, Irvine, CA 92697, USA, [d] Institute of Physics, Academy of Sciences of the Czech Republic, 182 21, Czech Republic, [e] CERN, CH-1211 Geneva, Switzerland, [f] Cornell University, Ithaca, NY 14853, USA, [g] University of Cyprus, Nicosia CY-1678, Cyprus, [h] Office of Science, U.S. Department of Energy, Washington, DC 20585, USA, [i] University College Dublin, Dublin 4, Ireland, [j] ETH, 8092 Zürich, Switzerland, [k] University of Fukui, Fukui City, Fukui Prefecture, Japan 910-0017, [l] Universidad Iberoamericana, Lomas de Santa Fe, México, C.P. 01219, Distrito Federal, [m] University of Iowa, Iowa City, IA 52242, USA, [n] Kinki University, Higashi-Osaka City, Japan 577-8502, [o] Kansas State University, Manhattan, KS 66506, USA, [p] Brookhaven National Laboratory, Upton, NY 11973, USA, [q] Istituto Nazionale di Fisica Nucleare, Sezione di Lecce, Via Arnesano, I-73100 Lecce, Italy, [r] Queen Mary, University of London, London, E1 4NS, United Kingdom, [s] University of Melbourne, Victoria 3010, Australia, [t] Muons, Inc., Batavia, IL 60510, USA, [u] Nagasaki Institute of Applied Science, Nagasaki 851-0193, Japan, [v] National Research Nuclear University, Moscow 115409, Russia, [w] Northwestern University, Evanston, IL 60208, USA, [x] University of Notre Dame, Notre Dame, IN 46556, USA, [y] Universidad de Oviedo, E-33007 Oviedo, Spain, [z] CNRS-IN2P3, Paris, F-75205 France, [aa] Universidad Tecnica Federico Santa Maria, 110v Valparaiso, Chile, [bb] Sejong University, Seoul 143-747, Korea, [cc] The University of Jordan, Amman 11942, Jordan, [dd] Universite catholique de Louvain, 1348 Louvain-La-Neuve, Belgium, [ee] University of Zürich, 8006 Zürich, Switzerland, [ff] Massachusetts General Hospital, Boston, MA 02114 USA, [gg] Harvard Medical School, Boston, MA 02114 USA, [hh] Hampton University, Hampton, VA 23668, USA, [ii] Los Alamos National Laboratory, Los Alamos, NM 87544, USA, [jj] Università degli Studi di Napoli Federico II, I-80138 Napoli, Italy

orders of the on-shell renormalization scheme [3], the $\sin^2\theta_W$ parameter is related to the W-boson mass M_W and the Z-boson mass M_Z by the relationship $\sin^2\theta_W = 1 - M_W^2/M_Z^2$. Radiative corrections alter the strength of the Born-level couplings into effective couplings. These effective couplings have been investigated at the Tevatron [4–7], at the LHC [8–10], and at LEP-1 and SLC [11, 12]. The on-shell $\sin^2\theta_W$ coupling has been investigated with neutrino-nucleon collisions at the Tevatron [13] and with electron-proton collisions at HERA [14].

The effective $\sin^2\theta_W$ coupling at the lepton vertex, denoted as $\sin^2\theta_{\rm eff}^{\rm lept}$, has been accurately measured at the LEP-1 and SLC e^+e^- colliders [11, 12]. The combined average of six individual measurements yields a value of 0.23149 ± 0.00016. However, there is tension between the two most precise individual measurements: the combined LEP-1 and SLD b-quark forward-backward asymmetry ($A_{\rm FB}^{0,{\rm b}}$) yields $\sin^2\theta_{\rm eff}^{\rm lept} = 0.23221 \pm 0.00029$, and the SLD left-right polarization asymmetry of Z-boson production ($\mathcal{A}_\ell$) yields $\sin^2\theta_{\rm eff}^{\rm lept} = 0.23098 \pm 0.00026$. They differ by 3.2 standard deviations.

The Drell-Yan process at hadron-hadron colliders is also sensitive to the $\sin^2\theta_{\rm eff}^{\rm lept}$ coupling. Measurements of the forward-backward asymmetry in the ℓ^- polar-angle distribution as a function of the lepton-pair invariant mass are used to extract the coupling. This paper presents a new measurement of the $\sin^2\theta_{\rm eff}^{\rm lept}$ coupling and an inference of the $\sin^2\theta_W$ parameter using a sample of e^+e^- pairs corresponding to an integrated $p\bar{p}$ luminosity of 9.4 fb^{-1} collected at the Tevatron $p\bar{p}$ collider. Innovative methods for the calibration of the electron energy and the measurement of the forward-backward asymmetry are used. Electroweak radiative corrections used for the extraction of $\sin^2\theta_{\rm eff}^{\rm lept}$ and $\sin^2\theta_W$ are derived from an approach used by LEP-1 and SLD.

An outline of the paper follows. Section II provides an overview of the lepton angular distributions and the extraction of $\sin^2\theta_{\rm eff}^{\rm lept}$. Section III discusses quantum chromodynamics (QCD) calculations for the forward-backward asymmetry and the inclusion of electroweak radiative-correction form factors used in the analysis of high-energy e^+e^- collisions. The form factors are required for the determination of $\sin^2\theta_W$ from the measurement of $\sin^2\theta_{\rm eff}^{\rm lept}$. Section IV describes the experimental apparatus. Section V reports on the selection of data. Section VI describes the simulation of the reconstructed data. Sections VII and VIII present the experimental calibrations and the measurement of the asymmetry, respectively, along with corresponding corrections to data and simulation. Section IX describes the method used to extract $\sin^2\theta_{\rm eff}^{\rm lept}$. Section X describes the systematic uncertainties. Section XI presents the results of this measurement using e^+e^- pairs and Sec. XII describes the combination of results from this measurement and a previous CDF measurement using $\mu^+\mu^-$ pairs [6]. Finally, Sec. XIII presents the summary. Standard units are used for numerical values of particle masses and momenta, e.g., 40 GeV/c^2 and 20 GeV/c, respectively, where c denotes the speed of light. Otherwise, natural units ($\hbar = c = 1$) are used.

II. LEPTON ANGULAR DISTRIBUTION

The angular distribution of leptons from the Drell-Yan process in the rest frame of the boson is governed by the polarization state of the γ^*/Z boson. In amplitudes at higher order than tree level, initial-state QCD interactions of the colliding partons impart to the γ^*/Z boson a momentum component transverse to the collision axis, thus affecting the polarization states.

In the laboratory frame, the $p\bar{p}$ collision axis is the z axis, with the positive direction oriented along the direction of the proton. The transverse component of any vector, such as the momentum vector, is defined to be relative to that axis. The transverse component of vectors in other reference frames is defined to be relative to the z axes in those frames.

For the description of the Drell-Yan process, the rapidity, transverse momentum, and mass of a particle are denoted as y, $P_{\rm T}$, and M, respectively. The energy and momentum of particles are denoted as E and $\vec{P}$, respectively. In a given coordinate frame, the rapidity is $y = \frac{1}{2}\,\ln[\,(E+P_{\rm z})/(E-P_{\rm z})\,]$, where $P_{\rm z}$ is the component of the momentum vector along the z axis of the coordinate frame.

The polar and azimuthal angles of the ℓ^- direction in the rest frame of the boson are denoted as ϑ and φ, respectively. For this analysis, the ideal positive z axis coincides with the direction of the incoming quark so that the definition of ϑ parallels the definition used in e^+e^- collisions at LEP [11, 12]. This frame is approximated by the Collins-Soper (CS) rest frame [15] for $p\bar{p}$ collisions. The rest frame is reached from the laboratory frame via two Lorentz boosts, first along the laboratory z-axis into a frame where the z component of the lepton-pair momentum vector is zero, followed by a boost along the transverse component of the lepton-pair momentum vector. A view of the CS frame is shown in Fig. 1.

The general structure of the Drell-Yan lepton angular-distribution in the boson rest frame consists of terms from nine helicity cross-sections that describe the polar-

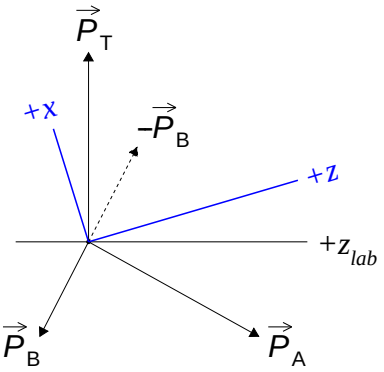

FIG. 1. Representation of the Collins-Soper coordinate axes (x, z) in the lepton-pair rest frame, along with the laboratory z axis (z_{lab}). The three axes are in the plane formed by the proton ($\vec{P}_A$) and antiproton ($\vec{P}_B$) momentum vectors in the rest frame. The z axis is the angular bisector of $\vec{P}_A$ and $-\vec{P}_B$. The y axis is along the direction of $\vec{P}_B \times \vec{P}_A$, and the x axis is in the direction away from the transverse component of $\vec{P}_A + \vec{P}_B$.

ization state of the boson,

$$\begin{aligned}\frac{dN}{d\Omega} \propto\ & (1+\cos^2\vartheta) + \\ & A_0\,\frac{1}{2}\,(1-3\cos^2\vartheta) + \\ & A_1\,\sin 2\vartheta\cos\varphi + \\ & A_2\,\frac{1}{2}\,\sin^2\vartheta\cos 2\varphi + \\ & A_3\,\sin\vartheta\cos\varphi + \\ & A_4\,\cos\vartheta + \\ & A_5\,\sin^2\vartheta\sin 2\varphi + \\ & A_6\,\sin 2\vartheta\sin\varphi + \\ & A_7\,\sin\vartheta\sin\varphi\,, \end{aligned} \tag{1}$$

where each term is relative to the cross section for unpolarized production integrated over the lepton angular distribution [16]. The coefficients A_{0-7} are functions of kinematic variables of the boson and vanish when the lepton-pair transverse momentum is zero, except for A_4, which contributes to the tree-level QCD amplitude and generates the forward-backward ℓ^- asymmetry in $\cos\vartheta$. Thus, at zero transverse momentum, the angular distribution reduces to the tree-level form $1+\cos^2\vartheta+A_4\cos\vartheta$. The A_4 coefficient is relatively uniform across the range of transverse momentum where the cross section is large (at values smaller than approximately 45 GeV/c), but slowly decreases for larger values of transverse momentum, where the cross section is very small. The A_0 and A_2 coefficients, corresponding to the longitudinal and transverse states of polarization, respectively, are the most significant and have been previously measured, along with A_3 and A_4 [17]. The A_1 coefficient, from the interference between the longitudinal and transverse states of polarization, is small in the CS frame. The A_{5-7} coefficients appear at second order in the QCD strong coupling, α_s, and are small in the CS frame [16]. Hereafter, the angles (ϑ, φ) and the angular coefficients A_{0-7} are intended to be specific to the CS rest frame.

The $A_4\cos\vartheta$ term violates parity, and is due to the interference of the amplitudes of the vector and axial-vector currents. Its presence induces an asymmetry in the φ-integrated $\cos\vartheta$ dependence of the cross section. Two sources contribute: the interference between the Z-boson vector and axial-vector amplitudes, and the interference between the photon vector and Z-boson axial-vector amplitudes. The asymmetric component from the γ^*-Z interference cross section contains g_A^f couplings that are independent of $\sin^2\theta_W$. The asymmetric component from Z-boson self-interference contains a product of g_V^f from the lepton and quark vertices, and thus is related to $\sin^2\theta_W$. At the Born level, this product is

$$T_3^\ell\,(1-4|Q_\ell|\sin^2\theta_W)\;T_3^q\,(1-4|Q_q|\sin^2\theta_W),$$

where ℓ and q denote the lepton and quark, respectively. For the Drell-Yan process, the relevant quarks are predominantly the light quarks u, d, or s. The coupling factor has an enhanced sensitivity to $\sin^2\theta_W$ at the lepton-Z vertex: for a $\sin^2\theta_W$ value of 0.223, a 1% variation in $\sin^2\theta_W$ changes the lepton factor (containing Q_ℓ) by about 8%, and it changes the quark factor (containing Q_q) by about 1.5% (0.4%) for the u (d or s) quark. Electroweak radiative corrections do not alter significantly this Born-level interpretation. Loop and vertex electroweak radiative corrections are multiplicative form-factor corrections to the couplings that change their values by a few percent [5].

The ℓ^- forward-backward asymmetry in $\cos\vartheta$ is defined as

$$A_{\rm fb}(M) = \frac{\sigma^+(M)-\sigma^-(M)}{\sigma^+(M)+\sigma^-(M)} = \frac{3}{8}A_4(M)\,, \tag{2}$$

where M is the lepton-pair invariant mass, σ^+ is the total cross section for $\cos\vartheta \geq 0$, and σ^- is the total cross section for $\cos\vartheta < 0$. Figure 2 shows the typical dependence of the asymmetry as a function of the lepton-pair invariant mass from a Drell-Yan QCD calculation. The offset of $A_{\rm fb}$ from zero at $M = M_Z$ is related to $\sin^2\theta_W$. Away from the Z pole, the asymmetry is dominated by the component from γ^*-Z interference, whose cross section is proportional to $(M^2 - M_Z^2)/M^2$, and the asymmetries in these regions are primarily related to the flux of partons. Consequently, the asymmetry distribution is sensitive to both $\sin^2\theta_W$ and the parton distribution functions (PDF) of the proton.

The $\sin^2\theta_{\rm eff}^{\rm lept}$ coupling is derived from the measurement of $A_{\rm fb}(M)$ and predictions of $A_{\rm fb}(M)$ for various input values of $\sin^2\theta_W$. Electroweak and QCD radiative corrections are included in the predictions of $A_{\rm fb}(M)$, with the electroweak radiative corrections derived from an approach adopted at LEP [18].

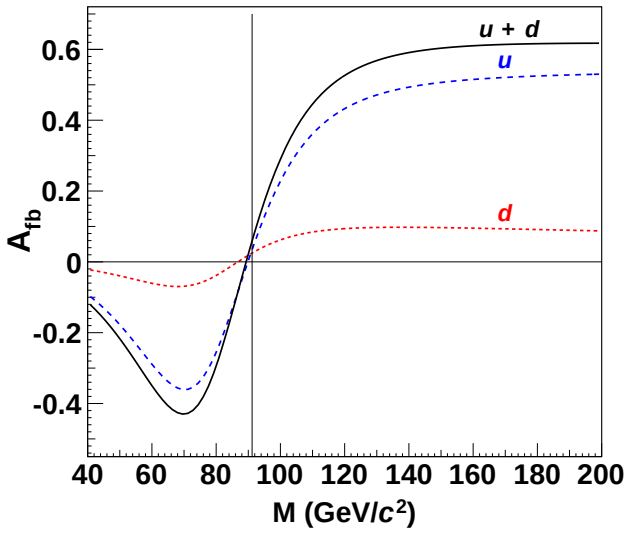

FIG. 2. Typical dependence of $A_{\rm fb}$ as a function of the lepton-pair invariant mass M. The label $u+d$ denotes the overall asymmetry, and the labels u and d denote the contribution to the overall asymmetry from quarks with charge $2/3$ and $-1/3$, respectively. The contribution of quarks categorized by the u or d label is $(\sigma_q^+ - \sigma_q^-)/\sigma$, where $q = u$ or d, $\sigma^{+(-)}$ their forward (backward) cross section, and σ the total cross section from all quarks. The vertical line is at $M = M_Z$.

III. ENHANCED QCD PREDICTIONS

Drell-Yan cross-section calculations with QCD radiation do not typically include electroweak radiative corrections. However, the QCD, quantum electrodynamic, and weak-interaction corrections can be organized to be individually gauge invariant so that they are applied as independent components.

Quantum electrodynamic (QED) radiative corrections that result in final-state photons are the most important for measurements derived from the Drell-Yan process, and they are included in the physics and detector simulation described in Sec. VI. The effects of QED radiation are removed from the measured distribution of $A_{\rm fb}$ using the simulation so that the measurement can be directly compared with QCD calculations of $A_{\rm fb}$ that do not include it.

The Drell-Yan process and the production of quark pairs in high-energy e^+e^- collisions are analogous processes: $q\bar{q} \to e^+e^-$ and $e^+e^- \to q\bar{q}$. At the Born level, the process amplitudes are of the same form except for the interchange of the electrons and quarks. Electroweak radiative corrections, calculated and extensively used for precision fits of LEP-1 and SLD measurements to the standard model [11, 12], are therefore applicable to the Drell-Yan process.

In the remainder of this section, the technique used to incorporate independently calculated electroweak radiative corrections for e^+e^- collisions into existing QCD calculations for the Drell-Yan process is presented.

A. Electroweak radiative corrections

The effects of virtual electroweak radiative corrections are incorporated into Drell-Yan QCD calculations via form factors for fermion-pair production according to $e^+e^- \to Z \to f\bar{f}$. The Z-amplitude form factors are calculated by ZFITTER 6.43 [18], which is used with LEP-1 and SLD measurement inputs for precision tests of the standard model [11, 12]. Corrections to fermion-pair production via a virtual photon include weak-interaction W-boson loops in the photon propagator, and Z-boson propagators at fermion-photon vertices; these corrections are not gauge-invariant except when combined with their gauge counterparts in the Z amplitude. The ZFITTER weak and QED corrections are organized to be separately gauge-invariant. Consequently, weak corrections to fermion-pair production via the virtual photon are included through the Z-amplitude form factors. ZFITTER uses the on-shell scheme [3], where particle masses are on-shell, and

$$\sin^2\theta_W = 1 - M_W^2/M_Z^2 \qquad (3)$$

holds to all orders of perturbation theory by definition. Since the Z-boson mass is accurately known (to ± 0.0021 GeV/c^2 [11, 12]), the inference of $\sin^2\theta_W$ is equivalent to an indirect W-boson mass measurement.

Form factors calculated by ZFITTER are tabulated for later use in QCD calculations. The specific standard-model assumptions and parameters used in the form-factor calculation are presented in the appendix, as well as their usage in the scattering amplitude A_q. The calculated form factors are ρ_{eq}, κ_e, κ_q, and κ_{eq}, where the label e denotes an electron and q denotes a quark. As the calculations use the massless-fermion approximation, the form factors only depend on the charge and weak isospin of the fermions. Consequently, the tabulated form factors are distinguished by three labels, e (electron type), u (up-quark type), and d (down-quark type). The form factors are complex valued, and are functions of the $\sin^2\theta_W$ parameter and the Mandelstam $\hat{s}$ variable of the $e^+e^- \to Z \to f\bar{f}$ process. The ρ_{eq}, κ_e, and κ_q form factors of the amplitude can be reformulated as corrections to the Born-level g_A^f and g_V^f couplings,

$$g_V^f \to \sqrt{\rho_{eq}}\,(T_3^f - 2Q_f\kappa_f \sin^2\theta_W) \text{ and}$$
$$g_A^f \to \sqrt{\rho_{eq}}\,T_3^f,$$

where f represents e or q.

The products $\kappa_f \sin^2\theta_W$, called effective-mixing terms, are directly accessible from measurements of the asymmetry in the $\cos\vartheta$ distribution. However, neither the $\sin^2\theta_W$ parameter nor the $\hat{s}$-dependent form factors can be inferred from measurements without assuming the standard model. The effective-mixing terms are denoted

as $\sin^2\theta_{\rm eff}$ to distinguish them from the on-shell definition of the $\sin^2\theta_W$ parameter of Eq. (3). The Drell-Yan process is most sensitive to the $\sin^2\theta_{\rm eff}$ term of the lepton vertex, $\kappa_e \sin^2\theta_W$. At the Z pole, κ_e is independent of the quark flavor, and the flavor-independent value of $\kappa_e \sin^2\theta_W$ is commonly denoted as $\sin^2\theta^{\rm lept}_{\rm eff}$. For comparisons with other measurements, the value of $\sin^2\theta^{\rm lept}_{\rm eff}$ at the Z pole is taken to be $\mathrm{Re}[\kappa_e(M_Z^2)]\sin^2\theta_W$.

B. QCD calculations

The ZFITTER form factors ρ_{eq}, κ_e, and κ_q are inserted into the Born g_A^f and g_V^f couplings of the Drell-Yan process. The κ_{eq} form factor is incorporated as an amplitude correction. This provides an enhanced Born approximation (EBA) to the electroweak terms of the amplitude. The form factor for the QED self-energy correction to the photon propagator is also part of the EBA. Complex-valued form factors are used in the amplitude. Only the electroweak-coupling factors in the QCD cross sections are affected. The standard LEP Z-boson resonant lineshape and the total decay width calculated by ZFITTER are used.

Both leading-order (LO) and next-to-leading-order (NLO) QCD calculations of $A_{\rm fb}$ for the process $p\bar{p} \to \gamma^*/Z \to \ell^+\ell^-$ are performed with form factors provided by ZFITTER. Two sets of PDFs are used to provide the incoming parton flux used in all QCD calculations discussed in this section, except where specified otherwise. They are the NLO CTEQ6.6 [19] PDFs and the next-to-next-to-leading order (NNLO) NNPDF-3.0 [20] PDFs. For consistency with the ZFITTER calculations, the NNPDFs selected are derived with a value of the strong-interaction coupling of 0.118 at the Z mass.

Two NLO calculations, RESBOS [21] and the POWHEG-BOX implementation [22] of the Drell-Yan process [23], are modified to be EBA-based QCD calculations. For both calculations, the cross section is finite as $P_{\rm T}^2$ vanishes. The RESBOS calculation combines a NLO fixed-order calculation at high boson $P_{\rm T}$ with the Collins-Soper-Sterman resummation formalism [24] at low boson $P_{\rm T}$, which is an all-orders summation of large terms from gluon emission calculated to next-to-next-to-leading log accuracy. The RESBOS calculation uses CTEQ6.6 NLO PDFs. The POWHEG-BOX calculation uses the NNLO NNPDF-3.0 PDFs, and is a fully unweighted partonic event generator that implements Drell-Yan production of $\ell^+\ell^-$ pairs at NLO. The NLO production implements a Sudakov form factor [25] that controls the infrared diverence at low $P_{\rm T}$, and is constructed to be interfaced with parton showering to avoid double counting. The PYTHIA 6.41 [26] parton-showering algorithm is used to produce the final hadron-level event. The combined implementation has next-to-leading log resummation accuracy. The LO calculations of $A_{\rm fb}$ are based on numerical integrations of the LO cross section using NNPDF-3.0 PDFs, and are used for direct comparisons with the POWHEG-BOX calculations.

The POWHEG-BOX NLO program, in conjunction with the NNPDF-3.0 NNLO PDFs, is chosen as the default EBA-based QCD calculation of $A_{\rm fb}$ with various input values of $\sin^2\theta_W$. The RESBOS calculation is used as a reference for resummed calculations. The LO calculation serves as a reference calculation for the sensitivity of $A_{\rm fb}$ to QCD radiation.

IV. EXPERIMENTAL APPARATUS

The CDF II apparatus is a general-purpose detector [27] at the Fermilab Tevatron, a $p\bar{p}$ collider with a center-of-momentum (cm) energy of 1.96 TeV. The positive-z axis of the detector coordinate system is directed along the proton direction. For particle trajectories, the polar angle $\theta_{\rm cm}$ is relative to the proton direction and the azimuthal angle $\phi_{\rm cm}$ is oriented about the beamline axis with $\pi/2$ being vertically upwards. The pseudorapidity of a particle is $\eta = -\ln\tan(\theta_{\rm cm}/2)$. Detector coordinates are specified as $(\eta_{\rm det}, \phi_{\rm cm})$, where $\eta_{\rm det}$ is the pseudorapidity relative to the detector center ($z = 0$).

The momentum $\vec{P}$ of a charged particle is measured in the magnetic spectrometer, which consists of charged-particle tracking detectors (trackers) immersed in a magnetic field. The energy of a particle is measured in the calorimeters surrounding the magnetic spectrometer. The component of momentum transverse to the beamline is $P_{\rm T} = |\vec{P}|\sin\theta_{\rm cm}$. The component of energy transverse to the beamline is $E_{\rm T} = E\sin\theta_{\rm cm}$.

The tracking detectors consist of a central tracker and an inner silicon tracker. The central tracker is a 3.1 m long, open-cell drift chamber [28] that extends radially from 0.4 to 1.4 m. Between the Tevatron beam pipe and the central tracker is a 2 m long silicon tracker [29]. Both trackers are immersed in a 1.4 T axial magnetic field produced by a superconducting solenoid just beyond the outer radius of the drift chamber. Combined, these two trackers provide efficient, high-resolution tracking and momentum measurement over $|\eta_{\rm det}| < 1.3$.

Outside the solenoid is the central barrel calorimeter [30, 31] that covers the region $|\eta_{\rm det}| < 1.1$. The forward end-cap regions, $1.1 < |\eta_{\rm det}| < 3.5$, are covered by the end-plug calorimeters [32–34]. The calorimeters are scintillator-based sampling calorimeters, which are segmented along their depth into electromagnetic (EM) and hadronic (HAD) sections, and transversely into projective towers. The EM calorimeter energy resolutions measured in test beams with electrons are $\sigma/E = 13.5\%/\sqrt{E_{\rm T}}$ for the central calorimeter, and $\sigma/E = 16\%/\sqrt{E} \oplus 1\%$ for the plug calorimeter, where the symbol $\oplus$ is a quadrature sum, and $E_{\rm T}$ and E are in units of GeV. Both the central and plug EM calorimeters have preshower and shower-maximum detectors for electromagnetic-shower identification and centroid measurements. The combination of the plug shower-

maximum detector and silicon tracker provides enhanced tracking coverage to $|\eta_{\rm det}| = 2.8$. However, as $|\eta_{\rm det}|$ increases for plug-region tracks, the transverse track-length within the magnetic field decreases, resulting in increasingly poor track-curvature resolution. Within the plug shower-maximum detector, $|\eta_{\rm det}| = 2.8$ corresponds to a radial extent from the beamline of 23 cm.

V. DATA SELECTION

The data set, collected over 2002–2011, is the full CDF Run II sample and consists of $p\bar{p}$ collisions corresponding to an integrated luminosity of 9.4 fb^{-1}. Section V A reports on the online selection of events (triggers) for the $A_{\rm fb}$ measurement. Section V B describes the offline selection of electron candidates, and Sec. V C describes the selection of electron pairs.

A. Online event selection

Electron candidates are selected from two online triggers, CENTRAL-18, and Z-NO-TRACK. The CENTRAL-18 selection accepts events containing at least one electron candidate with $E_{\rm T} > 18$ GeV in the central calorimeter region. Candidates are required to have electromagnetic shower clusters in the central calorimeters that are geometrically matched to tracks from the central tracker. Electron candidates for the Z-NO-TRACK selection have no track requirement and are only required to be associated with an electromagnetic shower cluster with $E_{\rm T} > 18$ GeV. The selection, which accepts events containing at least one pair of candidates located in any calorimeter region, is primarily for dielectrons in the plug-calorimeter region where online tracking is not available. It also accepts the small fraction of dielectron events that fail the track requirements of the CENTRAL-18 trigger.

B. Offline electron selection

After offline event reconstruction, the purity of the sample is improved with the application of CDF standard-electron identification and quality requirements [27]. Fiducial constraints are applied to ensure that the electrons are in well-instrumented regions, thus ensuring good-quality and predictable reconstruction performance. Each electron candidate is required to be associated with a track, to significantly reduce backgrounds. The track-vertex position along the beamline ($z_{\rm vtx}$) is restricted to be within the luminous region, $|z_{\rm vtx}| < 60$ cm. Overall, 3% of the $p\bar{p}$ luminous region along the beamline is outside this fiducial region.

Electron identification in the central calorimeter region is optimized for electrons of $P_{\rm T} > 10$ GeV/c [27]. It uses information from the central and silicon trackers, the longitudinal and lateral (tower) segmentation of the electromagnetic and hadronic calorimeter compartments, and the shower-maximum strip detector (CES) within the electromagnetic calorimeter. The highest quality of signal selection and background rejection is provided by the trackers in combination with the CES. An electron candidate must have shower clusters within the electromagnetic calorimeter towers and CES signals compatible with the lateral profile of an electromagnetic shower. A candidate must also be associated to a track that extrapolates to the three-dimensional position of the CES shower centroid. The transverse momentum of the particle associated with the track must be consistent with the associated electron shower $E_{\rm T}$ via an E/P selection when $P_{\rm T} < 50$ GeV/c [27]. For both the track matching in the CES and the E/P selection, allowances are included for bremsstrahlung energy-loss in the tracking volume, which on average is about 20% of a radiation length. The fraction of shower energy in the hadronic-calorimeter towers behind the tower cluster of the electromagnetic calorimeter must be consistent with that for electrons through an $E_{\rm HAD}/E_{\rm EM}$ requirement. These selections are more restrictive than those applied in the online selections described in Sec. V A.

Such an offline selection has high purity and is called the tight central electron (TCE) selection. To improve the selection efficiency of central-electron pairs, a looser selection, called the loose central electron (LCE) selection, is applied on the second electron candidate. The looser variant does not use transverse shower-shape constraints, the E/P constraint, or track matching in the CES. For track associations, the track is only required to project into the highest-energy calorimeter tower within the cluster of towers associated with the electromagnetic shower.

Electron identification in the plug calorimeter also uses tracker information, the longitudinal and lateral (tower) segmentation of the electromagnetic and hadronic calorimeter compartments, and the shower-maximum strip detector (PES) within the electromagnetic calorimeter. As the plug-calorimeter geometry differs from the central geometry, the details of the selection requirements differ.

The end-plug calorimeters, with sampling planes perpendicular to the beamline, have projective towers that are physically much smaller than the central calorimeter towers and vary in size [32]. The electromagnetic showers in the plug calorimeter are clustered into "rectangular" 3×3 detector-tower clusters centered on the highest-energy tower. Good radial containment of these showers is achieved. The preshower detector is the first layer of the plug-electromagnetic calorimeter and it is instrumented and read out separately. As there are approximately 0.7 radiation lengths of material in front of it, its energy is always included in the electromagnetic-cluster shower energy.

Tracks entering the plug calorimeters have limited geometrical acceptance in the central tracker for $|\eta_{\rm det}| > 1.3$.

The forward coverage of the silicon tracker is exploited with a dedicated calorimetry-seeded tracking algorithm called "Phoenix". It is similar to the central tracking-algorithm, where tracks found in the central tracker are projected into the silicon tracker and hits within a narrow road of the trajectory initialize the silicon track reconstruction. With the Phoenix algorithm, the track helix in the magnetic field is specified by the position of the $p\bar{p}$ collision vertex, the three-dimensional exit position of the electron into the PES, and a helix curvature. The collision vertex is reconstructed from tracks found by the trackers. The curvature is derived from the $E_{\rm T}$ of the shower in the electromagnetic calorimeter. Two potential helices are formed, one for each charge. The algorithm projects each helix into the silicon tracker to initialize the track reconstruction. If both projections yield valid tracks, the higher-quality one is selected. Depending on its vertex location along the beamline, a track traverses zero to eight layers of silicon. A Phoenix track is required to traverse at least three silicon layers and have at least three silicon hits. Eighty percent of the tracks traverse four or more silicon layers, and the average track acceptance is 94%.

An electron candidate in a plug calorimeter must have a shower cluster within the electromagnetic calorimeter towers, an associated PES signal compatible with the lateral profile of an electromagnetic shower, and a longitudinal profile, measured using $E_{\rm HAD}/E_{\rm EM}$, that is consistent with that expected for electrons. The candidate must also be associated with a Phoenix track. Neither a $P_{\rm T}$ nor an E/P selection requirement is applied because the track momentum determined by the Phoenix algorithm is correlated with the calorimeter energy. Charge misidentification is significant at large $|\eta_{\rm det}|$ because of the reduced track-helix curvature resolution. The resolution is inversely proportional to the track-exit radius at the PES, which varies from 23 to 129 cm.

As Drell-Yan high-$E_{\rm T}$ leptons are typically produced in isolation, the electron candidates are required to be isolated from other calorimetric activity. The isolation energy, $E_{\rm iso}$, is defined as the sum of $E_{\rm T}$ over towers within a 0.4 isolation cone in (η, ϕ) surrounding the electron cluster. The towers of the electron cluster are not included in the sum. For central-electron candidates, the isolation requirement is $E_{\rm iso}/E_{\rm T} < 0.1$, and for plug-electron candidates, it is $E_{\rm iso} < 4$ GeV.

C. Offline electron-pair event selection

Events are required to contain two electron candidates in either the central or plug calorimeters. These events are classified into three topologies, CC, CP, and PP, where C (P) denotes that the electron is detected in the central (plug) calorimeter. The electron kinematic variables are based on the electron energy measured in the calorimeters and on the track direction. The kinematic and fiducial regions of acceptance for electrons in the three topologies are described below.

1. Central–central (CC)
   (a) $E_{\rm T} > 25$ (15) GeV for electron 1 (2);
   (b) $0.05 < |\eta_{\rm det}| < 1.05$.
2. Central–plug (CP)
   (a) $E_{\rm T} > 20$ GeV for both electrons;
   (b) Central electron: $0.05 < |\eta_{\rm det}| < 1.05$;
   (c) Plug electron: $1.2 < |\eta_{\rm det}| < 2.8$.
3. Plug–plug (PP)
   (a) $E_{\rm T} > 25$ GeV for both electrons;
   (b) $1.2 < |\eta_{\rm det}| < 2.8$.

The CC topology consists of TCE-LCE combinations with asymmetric $E_{\rm T}$ selections on electrons 1 and 2, the electrons in the pair with the higher and lower $E_{\rm T}$, respectively. Either electron can be the TCE candidate, and its LCE partner can also be a TCE candiate because they are a subset of the LCE candidates. The asymmetric selection, an optimization from the previous measurement of electron angular-distribution coefficients [17], improves the acceptance. For the CP topology, the central electron candidate must pass the TCE selection. The PP-topology electron candidates are both required to be in the same end of the CDF II detector; Drell-Yan electrons of the PP topology on opposite ends of the CDF II detector are overwhelmed by QCD dijet backgrounds at low $P_{\rm T}$. In addition, the longitudinal separation of vertex positions of the associated tracks of the candidates is required to be within 4 cm of each other.

The measurement of $A_{\rm fb}$ is based on the direction of the e^- in the CS frame, and any charge misidentification dilutes the result. Charge misidentification is small for central tracks and significant for plug tracks. Consequently, only CC- and CP-topology pairs are used in the measurement. For the CP-topology, the central electron is used to identify the e^-. Electron pairs of the PP topology are only used for plug-calorimeter calibrations and cross checks. The same-charge pairs of the CC topology are also not used in the measurement, but they are used for calibrations, simulation tuning, and consistency checks.

Signal events intrinsically have no imbalance in the total energy in the transverse plane from undetected particles except for those within uninstrumented regions of the detector or from semileptonic decays of hadrons. The transverse energy imbalance $\not\!\!E_{\rm T}$ is the magnitude of $-\sum_i E^i_{\rm T}\hat{n}_i$, where the sum is over calorimeter towers, $\hat{n}_i$ is the unit vector in the azimuthal plane that points from the $p\bar{p}$ collision vertex to the center of the calorimeter tower i, and $E^i_{\rm T}$ is the corresponding transverse energy in that tower. Events with $\not\!\!E_{\rm T} < 40$ GeV are selected, therefore poorly reconstructed signal events, characterized by large $\not\!\!E_{\rm T}$, are removed. Only a very

small fraction of signal events is removed. About half of the background events containing leptonically decaying W-bosons are removed because they have large intrinsic $\not\!\!E_{\rm T}$ from neutrinos, which are undetected.

VI. SIGNAL SIMULATION

Drell-Yan pair production is simulated using the PYTHIA [35] Monte Carlo event generator and CDF II detector-simulation programs. PYTHIA generates the hard, leading-order QCD interaction $q\bar{q} \to \gamma^*/Z$, simulates initial-state QCD radiation via its parton-shower algorithms, and generates the decay $\gamma^*/Z \to \ell^+\ell^-$. The CTEQ5L [36] PDFs are used in the calculations. The underlying-event and boson-$P_{\rm T}$ parameters are derived from the PYTHIA configuration PYTUNE 101 (AW), which is a tuning to previous CDF data [35, 37, 38].

Generated events are first processed by the event simulation, and then followed by the CDF II detector simulation based on GEANT-3 and GFLASH [39]. The event simulation includes PHOTOS 2.0 [40, 41], which adds final-state QED radiation (FSR) to decay vertices with charged particles (e.g., $\gamma^*/Z \to ee$). The default implementation of PYTHIA plus PHOTOS (PYTHIA+PHOTOS) QED radiation in the simulation has been validated in a previous 2.1 fb^{-1} measurement of $\sin^2\theta^{\rm lept}_{\rm eff}$ using Drell-Yan electron pairs [5].

The PYTHIA+PHOTOS calculation is adjusted using the data and the RESBOS calculation. The generator-level $P_{\rm T}$ distribution of the boson is adjusted so that the shape of the reconstruction-level, simulated $P_{\rm T}$ distribution matches the data in two rapidity bins: $0 < |y| < 0.8$ and $|y| \geq 0.8$. For this adjustment, reconstructed ee pairs of all topologies (CC, CP, and PP) in the 66–116 GeV/c^2 mass region are used. The generator-level boson-mass distribution is adjusted with a mass-dependent K-factor. The K-factor is the ratio of the RESBOS boson-mass distribution calculated using CTEQ6.6 PDFs relative to the PYTHIA 6.4 [26] boson-mass distribution calculated using CTEQ5L PDFs. No kinematic restrictions are applied.

Standard time-dependent beam and detector conditions are incorporated into the simulation, including the p and $\bar{p}$ beamline parameters; the luminous region profile; the instantaneous and integrated luminosities per data-taking period; and detector component calibrations, which include channel gains and malfunctions. The simulated events are reconstructed, selected, and analyzed in the same way as the experimental data.

VII. DATA AND SIMULATION CORRECTIONS

In this section, time- and position-dependent corrections and calibrations to the experimental and simulated data are presented. They include event-rate normalizations of the simulation to the data, energy calibrations of both the data and simulation, and modeling and removal of backgrounds from the data. The detector has 1440 EM calorimeter towers, each with different responses over time and position within the tower. Many instrumental effects are correlated, and the overall correction and calibration process is iterative.

A. Event rate normalizations

The simulation does not model the trigger and reconstruction efficiences observed in the data with sufficient precision. Time-, detector-location-, and luminosity-dependent differences are observed. To correct the observed differences in rate between the data and simulation, a scale-factor event weight is applied to simulated events. The scale factor is the ratio of the measured offline-selection efficiencies observed in data to the simulation versus time, detector location, and instantaneous luminosity.

The base correction described above using measured efficiencies is inadequate for the $A_{\rm fb}$ measurement for two reasons: 1) due to the more stringent selection requirements for the efficiency measurements, the bin sizes for the time, position, and luminosity dependence are wide, and a finer resolution is needed; and 2) the Tevatron $p\bar{p}$ luminosity profile is difficult to simulate. The second-level correction uses event-count ratios between the data and simulation, or scale factors, as event weights. Events are required to pass all standard selection requirements and the ee-pair mass is required to be within the 66–116 GeV/c^2 range. Events are separated into the CC, CP, and PP topologies and corrected separately.

The time and luminosity dependencies are related. The distributions of the number of $p\bar{p}$ collision vertices in each event ($n_{\rm vtx}$) and the location of these vertices along the beamline ($z_{\rm vtx}$) changed significantly with improvements to the Tevatron collider. These distributions are inadequately simulated and are corrected separately. For the $n_{\rm vtx}$ correction, the data and simulation are grouped into 39 calibration periods, and the distribution corrected on a period-by-period basis. The correction of the $z_{\rm vtx}$ distribution is organized into a smaller set of seven time intervals corresponding to improvements in the Tevatron collider. The $z_{\rm vtx}$ distribution has an rms spread of 30 cm, and it needs to be simulated accurately because at large $|z_{\rm vtx}|$ the electron acceptance as a function of $E_{\rm T}$ changes significantly.

The second-level correction to remove detector-location dependencies is a function of $|\eta_{\rm det}|$. In the central calorimeter, the corrections are small. In the plug calorimeters, the corrections are larger and they correct the effects of tower-response differences between data and simulation near tower boundaries.

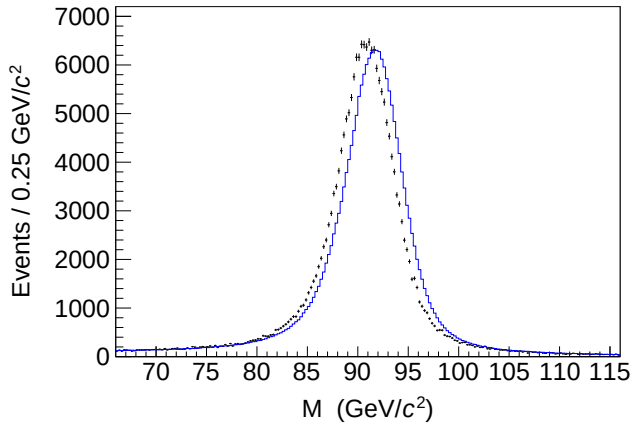

FIG. 3. Invariant ee-mass distribution for opposite-charged CC events prior to the calibration and background subtractions. The crosses are the data and the solid histogram is the simulation.

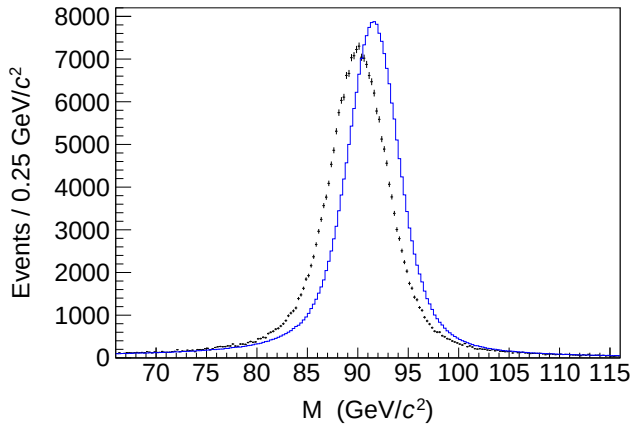

FIG. 4. Invariant ee-mass distribution for CP events prior to the calibration and background subtractions. The crosses are the data and the solid histogram is the simulation.

B. Energy calibrations

The energy calibrations are relative to the standard calibrations for time-dependent beam and detector conditions. Energy calibrations are multidimensional, and since it is not feasible to calibrate all components simultaneously, they are iteratively calibrated with a sequence of four steps using groups of lower dimension.

The standard calibrations for the calorimeter have energy-scale miscalibrations that depend on time and detector location, and range up to 5% in magnitude. The miscalibrations differ for the data and the simulation, and are larger at the edges of the plug calorimeter. The energy resolution of the simulation also needs additional tuning. Without any adjustments, the mass distributions of CC- and CP-topology electron pairs are as shown in Figs. 3 and 4, respectively.

Adjustments to correct the miscalibrations are constrained using the mass distributions of e^+e^- pairs about the Z pole. Calibration adjustments are based on three electron-pair mass distributions: 1) generator level, 2) simulated data, and 3) data. All three mass distributions are fit to a line shape that includes the Z-pole mass as a fit parameter. The Z-pole mass values obtained from fits to the experimental and simulated data are separately aligned to the corresponding generator-level value [42].

The generator-level mass is evaluated using clustered energies and includes the effects of QED FSR. The FSR electrons and photons are clustered about the seed tower in a manner similar to the clustering of electron reconstruction. The seed tower is based on the reconstructed electron, and the projection from the $p\bar{p}$ collision vertex to the tower is achieved by extrapolating the track helix. Since the detector acceptance slightly alters the lineshape of the mass distribution, generator-level events are selected by requiring that their kinematic properties after detector simulation meet all selection criteria.

The generator-level mass distribution is fit to the standard LEP Z-boson resonant line shape. The data and simulation mass distributions are fit to the standard LEP Z-boson resonant line shape convoluted with the resolution functions of the calorimeters, which are Gaussian. Typically, the fit range is ± 5 GeV/c^2 around the Z peak. The Z-pole mass and resolution width values are allowed to vary but the resonant width is fixed to the corresponding generator-level fit value. With this method, the resolution width values of the simulation and data are directly comparable and are used to calibrate the energy resolution of the simulation to the data.

Electron pairs of all topologies that satisfy the selection requirements are used in the calibration. The set of CC+PP events, and separately, of CP events, provides two independent sets of calibrations for all calorimeter components, such as towers. The electrons used to calibrate the energy scale of a component are denoted as reference electrons. The partners to these electrons can be anywhere in the detector so that miscalibrations of the current iteration are averaged out, and they also serve as references elsewhere. Energy-scale adjustments require the constraint of the sharp, nearly symmetric peak at the Z pole of the mass distribution. The energy distribution of the electrons is not as suitable because it is broad and asymmetric, and sensitive to the boson transverse-momentum and rapidity distributions, as well as the e^+e^- angular distribution.

The first step in an iteration is the time-dependent calibration of the overall energy scales for the central and plug calorimeters. Corrections are determined for each of the 39 calibration periods introduced in the previous section.

The next step is the relative calibration of calorimeter towers and the response maps within their boundaries. In this step, the bins are small and do not have enough events for accurate mass fits. Consequently, the energy response for each bin is quantified using the statistically more accurate mean of the scaled electron-pair

mass $M/(91.15\ \mathrm{GeV}/c^2)$ over the range 0.9–1.1, and is normalized to the overall average of the central or plug calorimeters. Tower-response corrections are important in the high $|\eta_{\mathrm{det}}|$ region of the plug calorimeters where standard calibrations are difficult. Corrections are determined for two time periods: calibration periods 0–17 and 18–39. Period 18 is the start of consistently efficient high-luminosity Tevatron operations, which commenced from April 2008. Both the central and plug calorimeter towers require additional response-map tuning at the periphery of the towers.

The third step calibrates the energy scales of the η-tower rings of the calorimeter. A ring consists of all towers in the ϕ dimension with the same $|\eta_{\mathrm{det}}|$ dimension. The adjustments from this step isolate the systematic variation of the energy scale in the η dimension of the standard calibration relative to the underlying physics. There are 22 η-tower rings, 12 of which are in the plug calorimeter. The lowest and highest η-tower rings of the plug calorimeter are not in the acceptance region. Separate calibrations for the CC+PP and CP data are iteratively determined using two passes, with corrections determined for two time periods, 0–17 and 18–39. First, the central and plug rings are calibrated with events from the CC+PP data. These calibrations are used only for CC- and PP-topology pairs. Then the CP data set calibration is derived from CP events, using the CC+PP calibrations as initial values for the calibration. The calibrations from the CC+PP and CP sets are expected to be slightly different due to the wide z_{vtx} distribution of $p\bar{p}$ collision vertices at the Tevatron. The geometry of an electron shower within the CDF calorimeters depends on the position of the collision vertex. Away from $z_{\mathrm{vtx}} = 0$, the transverse segmentation of the calorimeter is less projective, and the fraction of the shower energy sampled by the calorimeter is different. As the magnitude of z_{vtx} increases, the electron energy reconstructed in the calorimeter can change.

Accompanying the η-ring correction is the extraction of the underlying-event energy contained within an electron-shower cluster. The electron-pair mass distributions show an observable dependence on the number of $p\bar{p}$ collision vertices in an event. Assuming that the underlying-event energy per shower cluster increases linearly with n_{vtx}, these mass distributions are used to extract the associated underlying-event energy of a shower cluster per vertex for each η ring. For the central calorimeter, the value is approximately constant at 35 MeV. For the plug calorimeters, the value is approximately 150 MeV for $|\eta_{\mathrm{det}}| < 2$ and increases to 1.5 GeV at $|\eta_{\mathrm{det}}| \approx 2.8$. The expected underlying-event energy is subtracted from the measured electron energy.

The fourth step removes residual miscalibrations in both η_{det} and ϕ. The energy scales on a grid with 16 η_{det} and 8 ϕ_{cm} bins are calibrated, along with determinations of the corresponding energy resolutions. The η_{det} bins span both ends of the detector, with eight bins each for the central and plug calorimeters. Events in each $(\eta_{\mathrm{det}}, \phi_{\mathrm{cm}})$ bin are further divided into electron pairs with η_{det} values of the same sign (SS) and pairs with opposite-sign values (OS). There are differences of a few tenths of a percent between the SS- and OS-pair calibrations. The electrons of SS and OS pairs also have differing showering geometries within the calorimeters due to the wide z_{vtx} distribution of $p\bar{p}$ collisions. The fraction of SS pairs for the CC topology is approximately 50%. For the CP topology, the fraction varies with the η-bin index, and the range is approximately 50% to 80%. The PP-topology sample consists entirely of SS pairs.

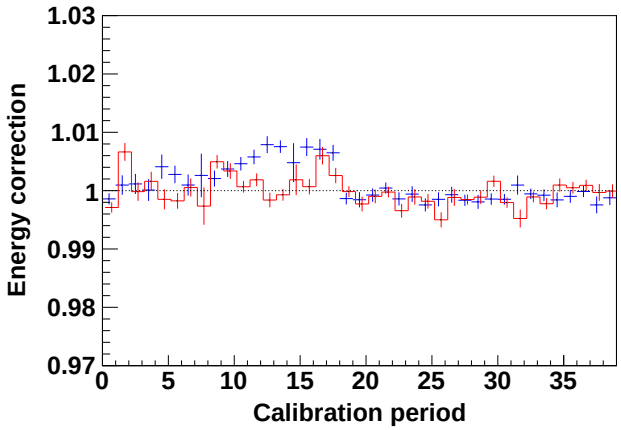

FIG. 5. Corrections to the global energy scales as functions of the calibration period for the data. The central calorimeter corrections are the crosses (blue), and for the plug calorimeter, the histogram (red) gives the corrections.

The energy resolution of the calorimeter simulation is also adjusted for each calibration bin of the fourth step. Line-shape fits to the mass distributions of the data and the simulation provide the resolution-smearing parameters σ_{d}^2 and σ_{s}^2, respectively. The fit values of σ_{d} are approximately 2 GeV/c^2 for all bins. For most bins, the simulation resolution is adjusted with an additional Gaussian rms deviation of $\sigma_{\mathrm{d}}^2 - \sigma_{\mathrm{s}}^2$. For 24% of the central bins, this value is negative, and the alternative is to rescale the simulation energy bias $\Delta E_{\mathrm{bias}} \equiv E_{\mathrm{gen}} - E_{\mathrm{rec}}$ of each event, where E_{gen} is the generator-level clustered energy and E_{rec} is the reconstruction-level energy. The resolution is modified by scaling the event-by-event bias with the factor f_{bias} so that the new reconstruction-level energy is $E_{\mathrm{gen}} - f_{\mathrm{bias}}\Delta E_{\mathrm{bias}}$. The value of f_{bias} does not deviate from its expected value of unity by more than 17%.

The energy calibration stabilizes after three iterations. The time-dependent global corrections to the energy scales of the central and plug calorimeters from step one are shown in Fig. 5. Approximately 20% of the data is contained in time periods 0–10, and 68% in time periods 18-38. The energy calibrations over η-tower rings from step three have the largest effect. Figure 6 shows the corrections derived from the CP calibration set for the two time periods, 0–17 and 18–38. The corrections de-

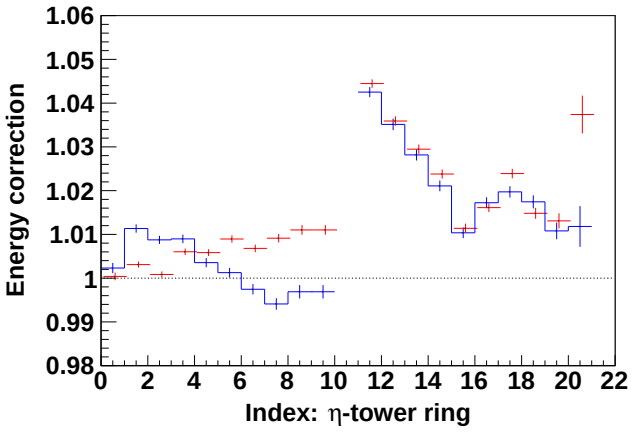

FIG. 6. Corrections to the energy scales as functions of the calorimeter η-tower ring index for the CP-topology data. The corrections from time periods 0 to 17 are represented by the histograms (blue), and those from time periods 18 to 38 by the crosses (red). The central calorimeter region is index 0 to 9. Index 21 towers are about 23 cm from the beamline.

rived from the CC+PP calibration set are similar. For the central calorimeter, the corrections from periods 0 to 17 and 18 to 38 are different because its standard calibration procedure was modified prior to the start of period 18. The tower-gain calibrations include an additional η-dependent correction that ranges from 0 to 2%. For periods 0–10 and 11–17, the central-calorimeter corrections are close to and compatible with the combined corrections shown in Fig. 6. The mass distributions of CC- and CP-topology electron pairs after the energy calibration adjustments, and other corrections presented next, are shown later in Figs. 12 and 13, respectively.

C. Backgrounds

The backgrounds are negligible in the Z-peak region used for the energy calibration but they are detectable in the low- and high-mass regions of the mass distributions. In this section, the level and shapes of the backgrounds in the ee-pair mass distribution are determined separately for each of the CC, CP, and PP topologies.

The backgrounds are from the production of QCD dijets, $Z \to \tau^+\tau^-$, W+jets, dibosons (WW, WZ, ZZ), and $t\bar{t}$ pairs. All backgrounds except for QCD are derived from PYTHIA [35] samples that are processed with the detector simulation, and in which the integrated luminosity of each sample is normalized to that of the data. The diboson and $t\bar{t}$ sample normalizations use total cross sections calculated at NLO [43]. The W+jets and $Z \to \tau^+\tau^-$ sample normalizations use the total cross sections calculated at LO multiplied by an NLO-to-LO K-factor of 1.4. Sample normalizations based on these calculated cross sections are referenced as default normalizations. Simulated events are required to pass all selections required of the data.

The QCD background is primarily from dijets that are misidentified as electrons. This background is extracted from the data assuming that its combination with the sum of the simulated signal and other backgrounds matches the observed mass distribution. The QCD background distribution, parametrized with level and shape parameters, is determined in a fit of the data to the sum of all backgrounds in conjunction with the simulated signal. The mass range for the fit is 42–400 GeV/c^2 with 50 equally spaced bins in $\ln M$, and the minimization statistic is the χ^2 between the data and the sum of predicted components over all bins. The normalizations of the simulated signal and backgrounds are also allowed to vary from their default values via scale factors. However, as most simulated backgrounds are very small, they are only allowed to vary within their normalization uncertainties. The constraint is implemented with an additional χ^2 term $(f_{\rm norm}-1)^2/0.085^2$, where $f_{\rm norm}$ is the scale factor of the background calculation. The uncertainty of the measured luminosity is 6% [44]; the prediction uncertainty is taken to be equally as large; and their combination gives the estimate for the constraint uncertainty of 0.085. The $t\bar{t}$, diboson, and W+jets backgrounds are always constrained. The $Z \to \tau^+\tau^-$ background is the second largest, and for CC-topology events, the scale factor is determined with the data. However, for CP- and PP-topology events, the $Z \to \tau^+\tau^-$ background scale factors are constrained to their default normalizations.

For the QCD-background analysis, two independent data samples are used: events passing the selection criteria and events failing them. The first sample, denoted as the signal sample, is used to determine the level of the QCD background and its shape over the mass distribution. The second sample, denoted as the QCD-background sample, is derived from events failing the selection criteria, and is for the event-by-event background subtractions from kinematic distributions.

Electron-like candidates for the QCD-background samples are selected by reversing criteria that suppress hadrons and QCD jets. One candidate passes all electron selection requirements except the isolation criterion. The other is required to be "jet-like" by reversing the isolation and $E_{\rm HAD}/E_{\rm EM}$ selection criteria. Since there is a small fraction of γ^*/Z events in the initial background sample, the reverse selections are optimized for each ee-pair topology to remove them. As the reversed selection criteria bias the mass distributions, events of these QCD-background samples are reweighted so that the overall normalization and the shapes of the mass distributions match those extracted from the signal samples.

For the CC topology, same-charge pairs passing the selection criteria are also used to determine the QCD background parameters, because 50%-60% of the events in the low- and high-mass regions are from QCD. The first step in the background determination is the extraction of the shape and default level of the QCD background

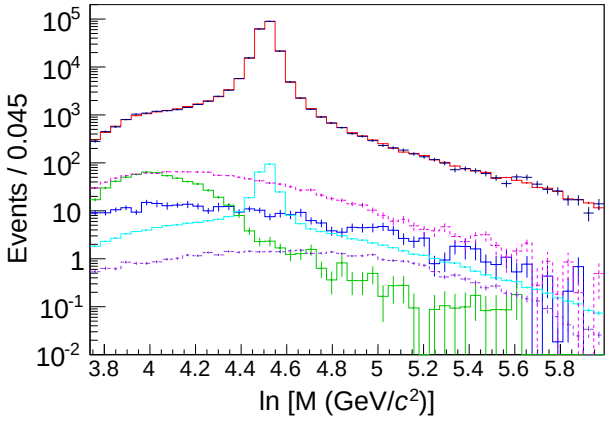

FIG. 7. Logarithmically binned mass distributions for oppositely charged ee-pair candiates in CC-topology events. The (black) crosses are the data, the (red) histogram overlapping the data is the sum of all components, the (green) histogram concentrated at lower masses is the $Z \to \tau^+\tau^-$ component, and the (cyan) histogram in the middle with the Z peak is the diboson component. The remaining broad distributions, from top to bottom, are QCD (magenta), W+jets (blue), and $t\bar{t}$ (purple). The comparison of the data with the sum of the components yields a χ^2 of 56 for 50 bins.

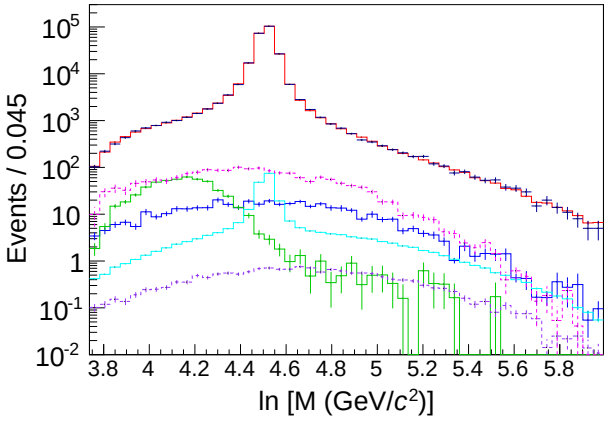

FIG. 8. Logarithmically binned mass distributions for CP-topology electron-pair candidates. The (black) crosses are the data, the (red) histogram overlapping the data is the sum of all components, the (green) histogram concentrated at lower masses is the $Z \to \tau^+\tau^-$ component, and the (cyan) histogram in the middle with the Z peak is the diboson component. The remaining broad distributions, from top to bottom are: QCD (magenta), W+jets (blue), and $t\bar{t}$ (purple). The comparison of the data with the sum of the components yields a χ^2 of 50 for 50 bins.

from the same-charge distribution. Then, the mass distributions of both same-charge and opposite-charge pairs passing the selection criteria are fit simultaneously for the background level parameters. The large fraction of QCD events in the same-charge distribution constrains the QCD background level parameter. Consequently, the scale factor for the normalization of the $Z \to \tau^+\tau^-$ background is determined using the data, but the default normalization is not accommodated. If the $Z \to \tau^+\tau^-$ normalization is allowed to vary, the fit determines a scale factor value of 0.53 ± 0.11. However, if the normalization is restricted via the constraint to the default value, the fit pulls the scale factor away from its default value of unity to a value of 0.83 ± 0.07, and the χ^2 increases by six units relative to the unconstrained fit. The detector simulation and event normalizations for the $Z \to \tau^+\tau^-$ sample, consisting of lower-$E_{\rm T}$ secondary electrons from τ decays, are not tuned. Consequently, the 0.53 value is chosen for the $A_{\rm fb}$ measurement and the 0.83 value is used as a systematic variation. The CC-topology opposite-charge mass distributions for the data, the simulated data plus backgrounds, and the backgrounds are shown in Fig. 7.

For the CP and PP topologies, the signal samples consist of both same- and opposite-charge electron pairs. Charge separation is not useful because of the significant charge misidentification rate for electrons in the plug region. The largest background in each topology is from QCD. However, the sum of all backgrounds is still small in relation to the signal. If all backgrounds are allowed to vary in the fits, the minimizations are underconstrained. Consequently, the simulated backgrounds are constrained to their default normalizations, and only the levels and shapes of the QCD backgrounds are varied. The shape of the QCD background for each topology is parametrized with an asymmetric-Gaussian function that consists of two piecewise continuous Gaussians joined at their common mean but with different widths. One of the function parameters is empirically tuned in the high- or low-mass region. As these regions have the largest level of backgrounds, it is important to control the fit within these regions. For the CP topology, the width on the high-mass side is first optimized in the region $M > 127$ GeV/c^2, and then the backgrounds and simulated signal are fit to the data. For the PP topology, the mean of the asymmetric-Gaussian is first optimized in the low-mass region in the vicinity of the mass threshold, and then the backgrounds and simulated signal are fit to the data. The CP- and PP-topology mass distributions for the data, the simulated data plus backgrounds, and the backgrounds are shown in Figs. 8 and 9, respectively.

The CC-, CP-, and PP-topology samples contain approximately 227 000, 258 000, and 80 000 events, respectively, within the 42–400 GeV/c^2 mass region. Table I summarizes the overall background levels for these samples. The total backgrounds for CC-, CP-, and PP-topology samples are 1.1%, 1.2%, and 2.1%, respectively. For the CC- and CP-topology samples shown in Figs. 7 and 8 respectively, the background fractions in the vicinity of the Z-pole mass are small, but away from the pole mass, the levels are larger and range from about 0.1% to about 10%.

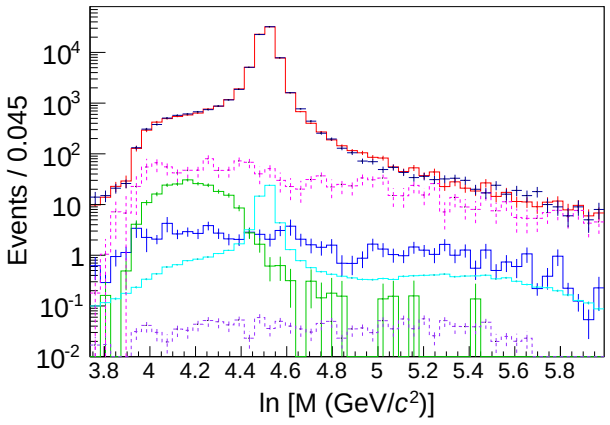

FIG. 9. Logarithmically binned mass distributions for PP-topology ee-pair candidates. The (black) crosses are the data, the (red) histogram overlapping the data is the sum of all components, the (green) histogram concentrated at lower masses is the $Z \to \tau^+\tau^-$ component, and the (cyan) histogram in the middle with the Z-peak is the diboson component. The remaining broad distributions, from top to bottom are: QCD (magenta), W+jets (blue), and $t\bar{t}$ (purple). The comparison of the data with the sum of the components yields a χ^2 of 69 for 50 bins.

TABLE I. Background fractions within the 42–400 GeV/c^2 mass region. The values with uncertainties are derived from the data.

Component	Background fraction (%)		
	CC	CP	PP
QCD	0.55±0.03	0.69 ± 0.13	1.64 ± 0.28
$Z \to \tau\tau$	0.26±0.06	0.21	0.27
W+jets	0.13	0.16	0.10
Diboson	0.14	0.10	0.08
$t\bar{t}$	0.02	0.01	0.01

VIII. THE $A_{\rm fb}$ MEASUREMENT

The Collins-Soper frame angle, $\cos\vartheta$ [15], is reconstructed using the following laboratory-frame quantities: the lepton energies, the lepton momenta along the beam line, the dilepton invariant mass, and the dilepton transverse momentum. The angle of the negatively charged lepton is

$$\cos\vartheta = \frac{l_+^- l_-^+ - l_-^- l_+^+}{M\sqrt{M^2 + P_{\rm T}^2}} ,$$

where $l_\pm = (E \pm P_z)$ and the $+$ $(-)$ superscript specifies that $l_\pm$ is for the positively (negatively) charged lepton. Similarly, the Collins-Soper expression for φ in terms of laboratory-frame quantities is

$$\tan\varphi = \frac{\sqrt{M^2 + P_{\rm T}^2}}{M} \frac{\vec{\Delta}\cdot\widehat{R}_{\rm T}}{\vec{\Delta}\cdot\widehat{P}_{\rm T}} ,$$

where $\vec{\Delta}$ is the difference between the ℓ^- and ℓ^+ momentum vectors; $\widehat{R}_{\rm T}$ is the transverse unit vector along $\vec{P}_p \times \vec{P}$, with $\vec{P}_p$ being the proton momentum vector and $\vec{P}$ the lepton-pair momentum vector; and $\widehat{P}_{\rm T}$ is the unit vector along the transverse component of the lepton-pair momentum vector. At $P_{\rm T} = 0$, the angular distribution is azimuthally symmetric. The defintions of $\cos\vartheta$ and $\tan\varphi$ are invariant under Lorentz boosts along the laboratory z direction.

$A_{\rm fb}$ is measured in 15 mass bins distributed over the range $50 < M < 350$ GeV/c^2. This section details the measurement method and presents the fully corrected measurement. Section VIII A describes a newly developed event-weighting technique. Section VIII B describes final calibrations and presents comparisons of the data and simulation. Section VIII C describes the resolution-unfolding technique and the corresponding covariance matrix of the unfolded $A_{\rm fb}$ measurement. Section VIII D describes the final corrections to the measurement and presents the fully corrected measurement of $A_{\rm fb}$.

A. Event-weighting method

The forward-backward asymmetry $A_{\rm fb}$ of Eq. (2) is typically determined in terms of the measured cross section $\sigma = N/(\mathcal{L}\,\epsilon A)$, where N is the number of observed events after background subtraction, $\mathcal{L}$ the integrated luminosity, ϵ the reconstruction efficiency, and A the acceptance within the kinematic and fiducial restrictions. The expression is

$$A_{\rm fb} = \frac{N^+/(\epsilon A)^+ - N^-/(\epsilon A)^-}{N^+/(\epsilon A)^+ + N^-/(\epsilon A)^-} ,$$

where the terms $N^{+(-)}$ and $(\epsilon A)^{+(-)}$ respectively represent N and ϵA for e^+e^- pairs with $\cos\vartheta \geq 0$ ($\cos\vartheta < 0$), and the common integrated luminosity is factored out. Systematic uncertainties common to $(\epsilon A)^+$ and $(\epsilon A)^-$ cancel out.

The asymmetry in this analysis is measured using the *event-weighting* method [45], which is equivalent to measurements of $A_{\rm fb}$ in $|\cos\vartheta|$ bins with these simplifying assumptions: $(\epsilon A)^+ = (\epsilon A)^-$ in each $|\cos\vartheta|$ bin, and Eq. (1) describes the angular distributions. As the interchange of the charge labels of the electrons transforms $\cos\vartheta$ to $-\cos\vartheta$, the detector assumption is equivalent to the postulate of a charge-symmetric detector for single electrons. For high $P_{\rm T}$ electrons with the same momenta, regions of the detector with charge-asymmetric acceptances and efficiencies are small. Thus, to first order, the acceptance and efficiency cancel out with the event-weighting method, and the small portions that do not cancel out are later corrected with the simulation (Sec. VIII D).

The measurement of $A_{\rm fb}$ within a $|\cos\vartheta|$ bin only de-

pends on the event counts $N^{\pm}$ and is

$$A'_{\rm fb} = \frac{N^+ - N^-}{N^+ + N^-} = \frac{8}{3} A_{\rm fb} \left(\frac{|\cos\vartheta|}{1+\cos^2\vartheta + \cdots} \right), \quad (4)$$

where $1+\cos^2\vartheta+\cdots$ denotes symmetric terms in Eq. (1). The event difference is proportional to $2A_4|\cos\vartheta|$, and the event sum to $2(1+\cos^2\vartheta+\cdots)$. Each bin is an independent measurement of $\frac{8}{3}A_{\rm fb}$, or equivalently, A_4, with an uncertainty of σ'/ξ, where σ' is the statistical uncertainty for $A'_{\rm fb}$, and ξ the angular factor in the parentheses of Eq. (4). When the measurements are combined, the statistical weight of each bin is proportional to ξ^2.

The binned measurements are reformulated into an unbinned, event-by-event weighted expression

$$A_{\rm fb} = \frac{N_n^+ - N_n^-}{N_d^+ + N_d^-}\,. \quad (5)$$

The $N_n^{\pm}$ and $N_d^{\pm}$ terms represent weighted event counts, and the subscripts n and d signify the numerator and denominator sums, respectively, which contain the same events but with different event weights. Consider the N^+ and N^- events of the binned measurement of $A'_{\rm fb}$ with a specific value of $|\cos\vartheta|$. In the unbinned measurement, their numerator and denominator weights contain: 1) factors to cancel the angular dependencies of their event difference ($N^+ - N^-$) and sum ($N^+ + N^-$), respectively, and 2) the ξ^2 factor for the statistical combination of these events with events from other angular regions. The method is equivalent to using a maximum-likelihood technique, and for an ideal detector the statistical precision of $A_{\rm fb}$ is expected to be about 20% better relative to the direct counting method [45]. However, detector resolution and limited acceptance degrade the ideal gain.

While the discussion of events weights illustrates an asymmetry measurement, the event weights presented in Ref. [45] and used in this analysis are for the measurement of the A_4 angular coefficient. The numerator and denominator event weights for the measurement of A_4 are $0.5\,|\cos\vartheta|/\omega^2$ and $0.5\cos^2\vartheta/\omega^3$, respectively, where ω is the symmetric $1+\cos^2\vartheta+\cdots$ term of Eq. 4.

The event weights are functions of the reconstructed kinematic variables $\cos\vartheta$, φ, and the lepton-pair variables M and $P_{\rm T}$. Only the A_0 and A_2 terms of Eq. (1) are used in the denominator of the angular factor of Eq. (4), and the angular coefficients are parametrized with

$$A_0 = A_2 = \frac{kP_{\rm T}^2}{kP_{\rm T}^2 + M^2}\,,$$

where k is a tuning factor for the $P_{\rm T}$ dependence of the A_0 and A_2 coefficients. For this analysis, $k = 1.65$, which is derived from a previous measurement of angular coefficients [17]. The exact form of these angular terms in the event weights is not critical for $A_{\rm fb}$ because the bulk of the events is at low boson $P_{\rm T}$.

The background events are subtracted from the weighted event sums on an event-by-event basis by assigning negative event weights when combining with the event sums.

The event-weighting method also does not compensate for the smearing of kinematic variables due to the detector resolution, and the restricted sampling of the asymmetry in kinematic regions with limited acceptance. Resolution-smearing effects are unfolded with the aid of the simulation, and sampling limitations are separately compensated.

B. Final calibrations

Relative to the expected asymmetry distribution illustrated in Fig. 2, the observed distribution is diluted by the detector resolution and QED FSR. The dilution from the detector resolution is visible in the vicinity of the Z-boson pole mass. The dilution from QED FSR is more pronounced at low masses because the rate of events produced in the vicinity of the Z-boson pole mass that radiate and are reconstructed in this low-mass region is more significant in relation to the intrinsic production rate. Detector miscalibrations add further distortions. All sources directly affect the electron-pair mass distributions that are primary inputs to the $A_{\rm fb}(M)$ distribution. The precision calibrations of both the data and simulation remove the additional distortions. In conjunction, the data-driven adjustments to the simulation remove differences between the data and simulation that impact the fully corrected $A_{\rm fb}(M)$ measurement.

The Collins-Soper $\cos\vartheta$ distribution for the simulation is also adjusted to improve agreement with the data. Only the symmetric part of the distribution is adjusted. The adjustments, determined for six electron-pair invariant mass bins whose boundaries are aligned with those used in the measurement, are determined from the ratios of the data-to-simulation $\cos\vartheta$ distributions. The ratios are projected onto the first five Legendre polynomials: $\Sigma_{i=0}^{i=4}\, p_i P_i(\cos\vartheta)$, where p_i are projection coefficients and $P_i(\cos\vartheta)$ are Legendre polynomials. The ratios are normalized so that the event count in the mass bin matches that of the data. The symmetric parts of the projections describe the ratios well and are used as the adjustments. Separate adjustments are applied to the CC- and CP-topology electron pairs as event weights. The corrections are a few percent or smaller in regions where the acceptance is large.

Figure 10 shows the $\cos\vartheta$ distributions after all calibrations for the combination of the CC and CP topologies and for the CC topology alone. The CP-topology dielectrons are dominant at large $|\cos\vartheta|$ and significantly reduce the statistical uncertainty of the measurement. Figure 11 shows the Collins-Soper φ distribution.

The CC- and CP-topology electron-pair mass distributions in the range of 66–116 GeV/c^2 are shown in Figs. 12 and 13, respectively. For PP-topology electron pairs with masses in the same range, the comparison of the simulation with the data yields a χ^2 of 232 for 200 bins.

The electron $E_{\rm T}$ distributions of the data are reasonably well described by the simulation. Figure 14 shows

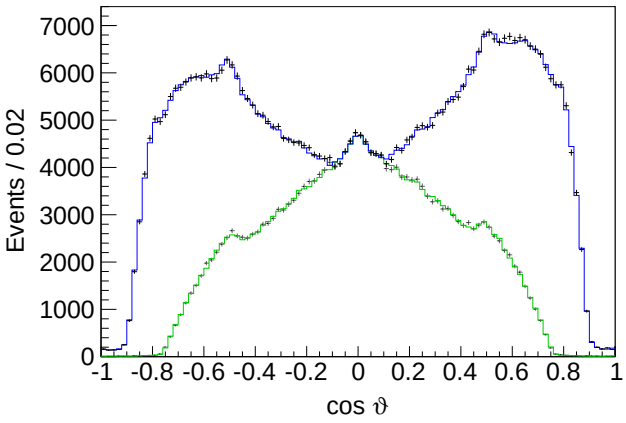

FIG. 10. Distributions of $\cos\vartheta$ in the Collins-Soper frame for dielectrons with $66 < M < 116$ GeV/c^2. The crosses are the background-subtracted data and the histograms are simulated data. The upper pair of crosses and histogram is from the combination of the CC and CP topologies, and the lower pair is the contribution from the CC topology only.

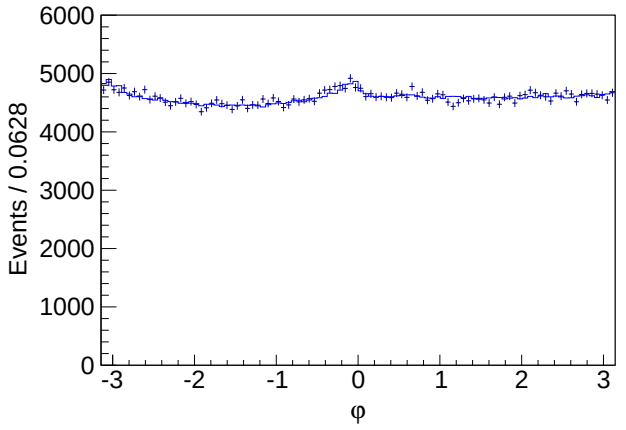

FIG. 11. Distibution of φ in the Collins-Soper frame for CC- and CP-topology dielectrons with $66 < M < 116$ GeV/c^2. The crosses are the background-subtracted data and the solid histogram is the simulation.

the $E_{\rm T}$ distribution of the electron with the higher $E_{\rm T}$ for CC-topology dielectrons for both the data and the simulation. Figure 15 shows the equivalent distribution for CP-topology electrons; here the electron can either be the central or plug electron.

The mass distribution of CC same-charge dielectrons has a clear Z-boson peak from charge misidentification. Figure 16 shows the CC same-charge mass distribution of the data and the simulation. This figure confirms that charge misidentification is reproduced well by the detector simulation. The misidentification rate per central electron is 0.6%. Charge misidentification on the central electron of CP pairs is thus expected to be small and properly simulated.

Charge misidentification, other categories of event mis-

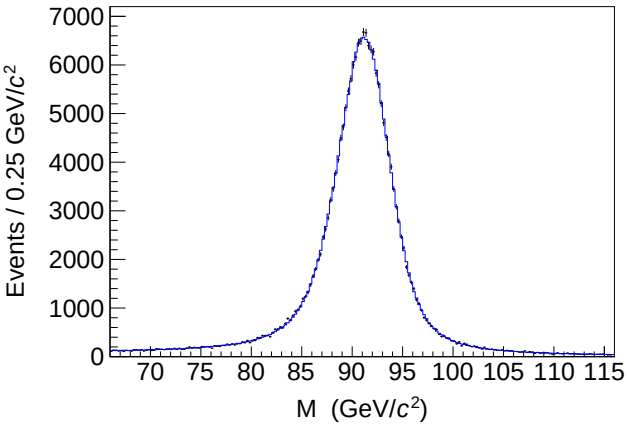

FIG. 12. Invariant ee-mass distribution for opposite-charged CC events. The crosses are the background-subtracted data and the solid histogram is the simulation. The comparison of the simulation with the data yields a χ^2 of 214 for 200 bins.

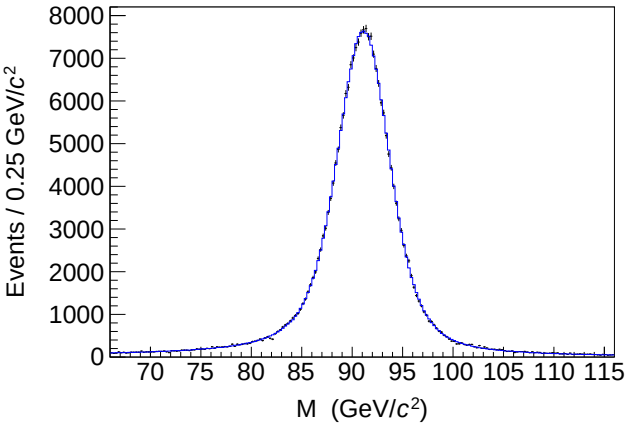

FIG. 13. Invariant ee-mass distribution for CP events. The crosses are the background-subtracted data and the solid histogram is the simulation. The comparison of the simulation with the data yields a χ^2 of 235 for 200 bins.

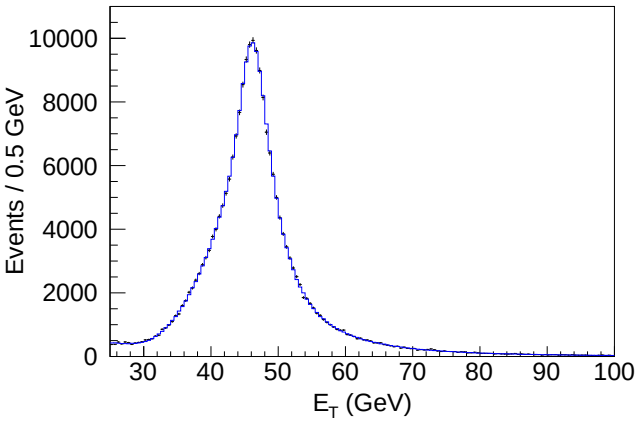

FIG. 14. $E_{\rm T}$ distribution for the CC-topology electron with the larger $E_{\rm T}$. The crosses are the background-subtracted data and the solid histogram is the simulation.

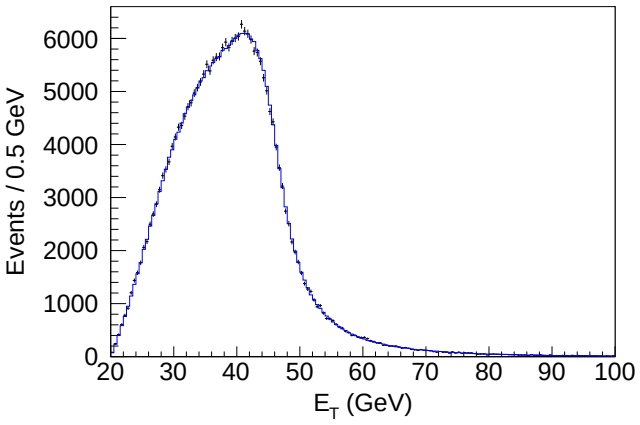

FIG. 15. $E_{\rm T}$ distribution for the CP-topology electron with the larger $E_{\rm T}$. The crosses are the background-subtracted data and the solid histogram is the simulation.

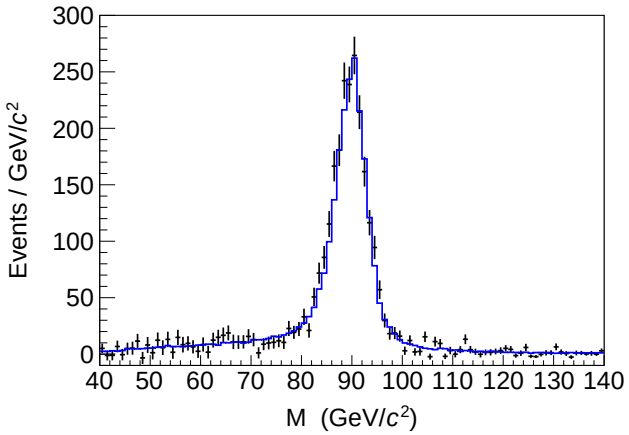

FIG. 16. Invariant ee-mass distribution for same-charge CC events. The crosses are the background-subtracted data and the solid histogram is the simulation.

reconstruction, and detector resolution affect the observed value of $\cos\vartheta$. The bias of the observed value, $\Delta\cos\vartheta$, obtained from the simulation, is defined as the difference between its true value prior to the application of QED FSR and the observed value. The measurement of $A_{\rm fb}$ is in turn biased by the fraction of events for which the sign of the observed $\cos\vartheta$ differs from the true value; this change of sign is denoted by sign-reversed $\cos\vartheta$. The bias distribution consists of a narrow central core of well reconstructed events, and a very broad distribution from events where the electron kinematic properties are poorly reconstructed. Charge misidentification reverses the sign of $\cos\vartheta$. If events with charge misidentification are excluded, the bias distributions of CC- and CP-topology events have narrow non-Gaussian central cores centered at zero with 95% of the events being contained within the range $|\Delta\cos\vartheta| < 0.006$. For opposite-charge CC-topology events, the effects of detector resolution dominate the bias. The fraction of events with

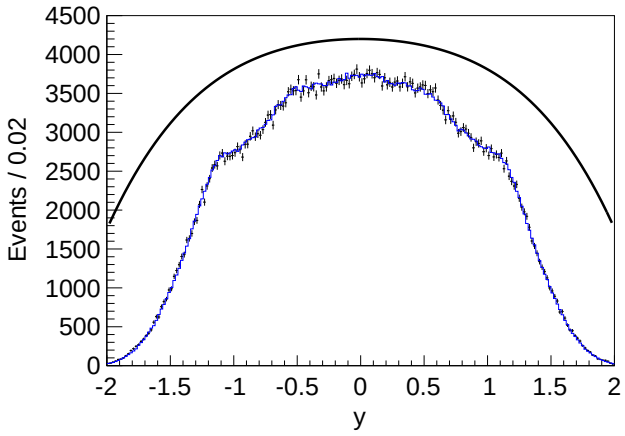

FIG. 17. Rapidity distribution of electron pairs from the CC and CP topologies with $66 < M < 116$ GeV/c^2. The crosses are the background-subtracted data and the histogram is the simulation. The upper curve is the (arbitrarily normalized) shape of the underlying rapidity distribution from PYTHIA. The measurement of $A_{\rm fb}$ is restricted to be within the region $|y| < 1.7$.

sign-reversed $\cos\vartheta$ is 0.3%, with most of the events being within the range $|\cos\vartheta| < 0.1$. For CP-topology events, the misidentification of the central-electron charge dominates the fraction of events with sign-reversed $\cos\vartheta$. The fraction decreases in value from 0.6% to 0.2% as $|\cos\vartheta|$ increases from 0.2 to 0.8. The measurement resolution of $\cos\vartheta$ consists of multiple components but their effects are small.

The rapidity distribution of electron pairs for the asymmetry measurement is shown in Fig. 17, along with the shape the underlying rapidity distribution from PYTHIA. At large values of $|y|$, the detector acceptance is significantly reduced. For increasing values of $|y|$ in the $|y| \gtrsim 1$ region, the asymmetry slowly changes. This change can only be tracked by event-weighting method if it has the events to do so. Consequently, the measurement of $A_{\rm fb}$ is restricted to the kinematic region $|y| < 1.7$. QCD calculations of $A_{\rm fb}$ used for comparisons with the measurement are similarly restricted. The electron-pair mass range of the measurement, 50 to 350 GeV/c^2, corresponds to maximum $|y|$ values of 3.7 to 1.7, respectively.

C. Resolution unfolding

After applying the calibrations and corrections to the experimental and simulated data, the asymmetry is measured in 15 bins of the electron-pair invariant mass. The bin boundaries are 50, 64, 74, 80, 84, 86, 88, 90, 92, 94, 96, 100, 108, 120, 150, and 350 GeV/c^2. The 50–64 and 150–350 GeV/c^2 bins are referenced in plots as the underflow and overflow bins, respectively, because they include candidates reconstructed with masses outside the range of the plot. This measurement, denoted as raw because

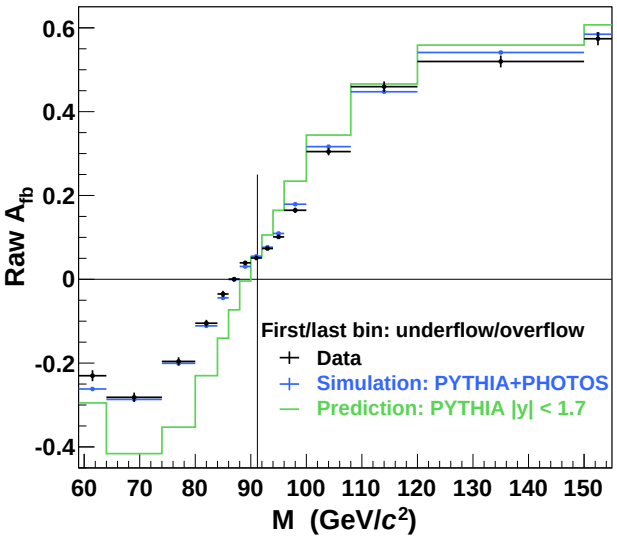

FIG. 18. Raw $A_{\rm fb}$ measurement in bins of the electron-pair invariant mass. The vertical line is at $M = M_Z$. Only statistical uncertainties are shown. The PYTHIA prediction for $|y| < 1.7$ does not include the effects of QED FSR.

the effects of the detector resolution and final-state QED radiation are not removed, is shown in Fig. 18. As the mass resolution smearing of the calorimeter in the vicinity of the Z-boson mass has an rms of approximately 2 GeV/c^2, the calibrations and tuning of the data and simulation are important for the resolution unfolding.

The CC and CP events have different geometries and resolutions so they are kept separate in the event-weighting phase and the unfolding phase. They are combined for the $A_{\rm fb}$ measurement and calculation of the measurement covariance matrix.

The unfolding of the resolution and QED FSR uses the event transfer matrices from the simulation, denoted by $\bar{n}_{gr}$. All data-driven corrections to the simulation are included. The symbol $\bar{n}_{gr}$ identifies the number of selected events that are generated in the electron-pair $(M, \cos\vartheta)$ bin g and reconstructed in the $(M, \cos\vartheta)$ bin r. In addition to the 15 mass bins, the forward-backward asymmetry has two angular regions, $\cos\vartheta \geq 0$, and $\cos\vartheta < 0$. Square transfer matrices for 30-element state vectors are implemented. The first 15 elements of the vectors are the mass bins for the $\cos\vartheta \geq 0$ angular region, and the remainder for the other angular region.

The simulation predicts significant bin-to-bin event migration among the mass bins when the produced and reconstructed values of $\cos\vartheta$ have the same sign. For a mass bin, there is very little migration of events from one angular region to the other. As the simulation sample size is normalized to the integrated luminosity of the data, the transfer matrices provide properly normalized estimates of event migration between bins. An estimator for the true unfolding matrix is $\bar{U}_{gr} = \bar{n}_{gr}/\bar{N}_r$, where $\bar{N}_r = \sum_g \bar{n}_{gr}$ is the expected total number of weighted events reconstructed in bin r. The 30-element state vector for $\bar{N}_r$ is denoted as $\vec{N}_r$, and the matrix $\bar{U}_{gr}$ by $\boldsymbol{U}$. The estimate for the resolution-unfolded state vector of produced events is $\vec{N}_g = \boldsymbol{U} \cdot \vec{N}_r$.

For the event-weighting method, there are two transfer matrices that correspond to the weighted-event counts N_n and N_d of Eq. (5), and thus two separate unfolding matrices $\boldsymbol{U}$, two separate event-weighted measurements of $\vec{N}_r$, and two separate estimates of the resolution-unfolded $\vec{N}_g$. The CC- and CP-event estimates of $\vec{N}_g$ for the numerator and denominator of $A_{\rm fb}$ are summed prior to the evaluation of $A_{\rm fb}$. The measurements of $A_{\rm fb}$ for the 15 mass bins are collectively denoted by $\vec{A}_{\rm fb}$.

The covariance matrix of the $A_{\rm fb}$ measurement, denoted by $\boldsymbol{V}$, is calculated using the unfolding matrices, the expectation values of $\vec{N}_r$ and $\vec{A}_{\rm fb}$ from the simulation, and their fluctuations over an ensemble. The per-experiment fluctuation to $\vec{N}_g$ is $\boldsymbol{U} \cdot (\vec{N}_r + \delta\vec{N}_r)$, where $\delta\vec{N}_r$ represents a fluctuation from the expectation $\vec{N}_r$. The variation $\delta\vec{A}_{\rm fb}$ resulting from the $\vec{N}_g$ fluctuation is ensemble-averaged to obtain the covariance matrix

$$V_{lm} = \langle\, (\delta\vec{A}_{\rm fb})_l (\delta\vec{A}_{\rm fb})_m \,\rangle\,,$$

where $(\delta\vec{A}_{\rm fb})_k$ ($k = l$ and m) denotes the kth element of $\delta\vec{A}_{\rm fb}$. Each element i of $\vec{N}_r$ undergoes independent, normally distributed fluctuations with a variance equal to the value expected for $\bar{N}_i$. Because $\bar{N}_i$ is a sum of event weights, fluctuations of $\bar{N}_i$ are quantified with the variance of its event weights. The two $\vec{N}_r$ vectors, the numerator vector and the denominator vector, have correlations. Elements i of the numerator and denominator vectors contain the same events, the only difference being that they have different event weights. To include this correlation, the event-count variations of elements i of the numerator and denominator $\delta\vec{N}_r$ vectors are based on the same fluctuation from a normal distribution with unit rms dispersion.

The covariance matrix is expanded and inverted to the error matrix using singular-value decomposition methods. As the covariance matrix is a real-valued symmetric 15×15 matrix, its 15 eigenvalues and eigenvectors are the rank-1 matrix components in the decomposition of the covariance matrix and the error matrix

$$\begin{aligned} \boldsymbol{V} &= \sum_n \lambda_n\, |v_n\rangle\langle v_n| \text{ and} \\ \boldsymbol{V}^{-1} &= \sum_n \lambda_n^{-1}\, |v_n\rangle\langle v_n|\,, \end{aligned} \tag{6}$$

where λ_n and $|v_n\rangle$ are the eigenvalues and eigenvectors of $\boldsymbol{V}$, respectively, and $|v_n\rangle\langle v_n|$ represents a vector projection operator in the notation of Dirac bra-kets.

The covariance matrix can have eigenvalues that are very small relative to the largest eigenvalue. Their vector projection operators select the fine structure of the resolution model, and at a small enough eigenvalue, they become particular to the simulation and include

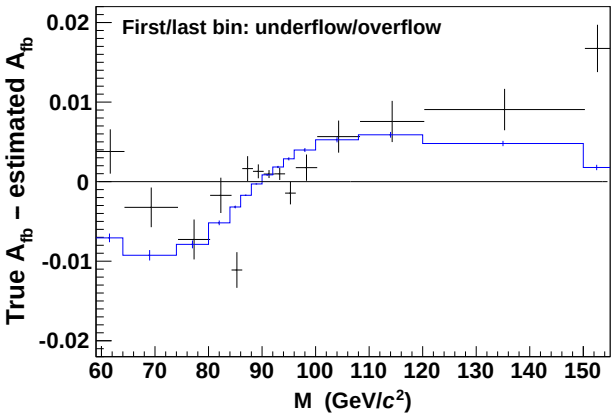

FIG. 19. Event-weighting bias in bins of the electron-pair invariant mass. The biases are the crosses, and the uncertainties are the bin-by-bin unfolding estimates of the simulation. The superimposed histogram is the difference between the $A_{\rm fb}$ calculations for the rapidity range $|y| < 1.7$ and $|y| < 1.5$, and the uncertainties are estimates for the PDF uncertainty.

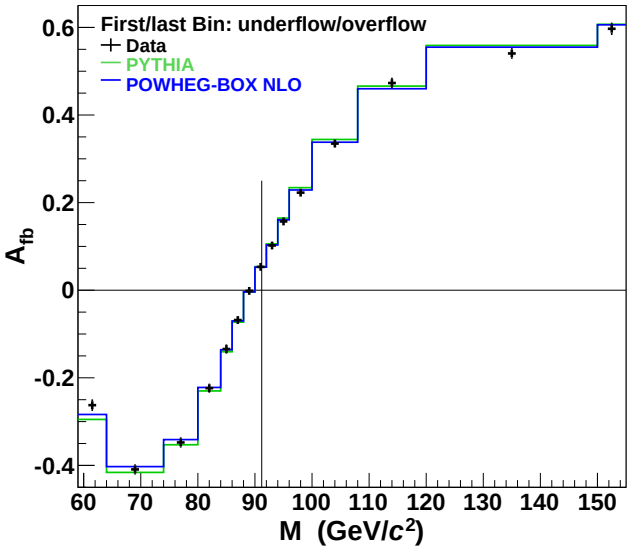

FIG. 20. Fully corrected $A_{\rm fb}$ for electron pairs with $|y| < 1.7$. The measurement uncertainties are bin-by-bin unfolding estimates. The vertical line is $M = M_Z$. The PYTHIA calculation uses $\sin^2\theta^{\rm lept}_{\rm eff} = 0.232$. The EBA-based POWHEG-BOX calculation uses $\sin^2\theta_W = 0.2243$ ($\sin^2\theta^{\rm lept}_{\rm eff} = 0.2325$) and the default PDF of NNPDF-3.0.

noise. While their contribution to the covariance matrix is small, they completely dominate the error matrix. The fine structures of the simulation, measurement, and calculation are different. Consequently, comparisons between the $A_{\rm fb}$ measurement and predictions that use the error matrix are unstable. To alleviate these instabilities, the decomposition of the error matrix, Eq. (6), is *regulated* so that the contributions of eigenvectors with very small eigenvalues are suppressed. A general method, as described below, is to add a regularization term or function r_n to the eigenvalues: $\lambda_n \to \lambda_n + r_n$, where $\lambda_n + r_n$ is the regularized eigenvalue.

D. Event-weighting bias correction

After resolution unfolding, the event-weighted $A_{\rm fb}$ values have second-order acceptance and efficiency biases from regions of limited boson acceptance, and to a lesser extent, from detector nonuniformities resulting in $(\epsilon A)^+ \neq (\epsilon A)^-$. The bias is defined as the difference between the true value of $A_{\rm fb}$ before QED FSR calculated with PYTHIA and the unfolded simulation estimate. The size of the simulation sample is 21 times that of the data. The bias is a mass-bin-specific additive correction to the unfolded $A_{\rm fb}$ measurement, and is shown in Fig. 19. All significant bias corrections are less than 8% of the magnitude of $A_{\rm fb}$ and most of them are 3% or less.

Figure 19 also shows the difference between asymmetries calculated with the measurement rapidity range $|y| < 1.7$, and with a reduced range $|y| < 1.5$. The difference is representative of contributions to the bias from regions of reduced acceptance at large values of $|y|$, and the PDF uncertainty of the difference is specified later in Sec. X A. For increasing values of $|y|$, there is a relative increase of the u- to d-quark flux and a decrease of the antiquark flux from the proton.

TABLE II. Fully corrected $A_{\rm fb}$ measurement for electron pairs with $|y| < 1.7$. The measurement uncertainties are bin-by-bin unfolding estimates.

Mass bin (GeV/c^2)	$A_{\rm fb}$
50–64	-0.262 ± 0.014
64–74	-0.409 ± 0.015
74–80	-0.348 ± 0.015
80–84	-0.224 ± 0.014
84–86	-0.134 ± 0.014
86–88	-0.068 ± 0.010
88–90	-0.0015 ± 0.0044
90–92	0.0533 ± 0.0017
92–94	0.1021 ± 0.0036
94–96	0.1570 ± 0.0087
96–100	0.2228 ± 0.0094
100–108	0.335 ± 0.010
108–120	0.473 ± 0.012
120–150	0.541 ± 0.012
150–350	0.597 ± 0.014

The covariance matrix of the bias-correction uncertainties is combined with the covariance matrix for the $A_{\rm fb}$ measurement. The fully corrected measurement of $A_{\rm fb}$, including the bias correction, is shown in Fig. 20 and tabulated in Table II.

IX. EXTRACTION OF $\sin^2\theta_{\rm eff}^{\rm lept}$

The Drell-Yan asymmetry measurement is directly sensitive to the effective-mixing terms $\sin^2\theta_{\rm eff}$, which are products of the form-factor functions with the static $\sin^2\theta_W$ parameter (Sec. III A). The asymmetry is most sensitive to the value of the effective-leptonic $\sin^2\theta_{\rm eff}$ term in the vicinity of the Z pole, or $\sin^2\theta_{\rm eff}^{\rm lept}$, and its value is derived from the $\sin^2\theta_W$ parameter of the $A_{\rm fb}$ template that best describes the measurement. For non-EBA calculations such as PYTHIA, the template parameter is $\sin^2\theta_{\rm eff}^{\rm lept}$. While the value of $\sin^2\theta_{\rm eff}^{\rm lept}$ is a direct measurement, the interpretation of the corresponding value of $\sin^2\theta_W$ and the form factors are dependent on the details of the EBA model.

The measurement and templates are compared using the χ^2 statistic evaluated with the $A_{\rm fb}$ measurement error matrix. Each template corresponds to a particular value of $\sin^2\theta_W$ and provides a scan point for the χ^2 function: $\chi^2(\sin^2\theta_W)$. The χ^2 values of the scan points are fit to a parabolic χ^2 function,

$$\chi^2(\sin^2\theta_W) = \bar{\chi}^2 + (\sin^2\theta_W - \overline{\sin^2}\theta_W)^2/\bar{\sigma}^2\,, \quad (7)$$

where $\bar{\chi}^2$, $\overline{\sin^2}\theta_W$, and $\bar{\sigma}$ are parameters. The $\overline{\sin^2}\theta_W$ parameter is the best-fit value of $\sin^2\theta_W$, $\bar{\sigma}$ is the corresponding measurement uncertainty, and $\bar{\chi}^2$ is the associated goodness-of-fit between the $A_{\rm fb}$ measurement and calculation over the 15 mass bins.

Without regularization of the error matrix, there are large fluctuations of the χ^2 values for each scan point from the expected parabolic form. Such fluctuations are induced by the small eigenvalue terms in the expansion of the error matrix, described in Eq. (6). To attenuate these fluctuations, the regularization function method described at the end of Sec. VIII C is used. The eigenvalues and regularization terms are shown in Fig. 21. The horizontal line of Fig. 21 is an estimate, detailed next, of the resolving power of the measurement. The eigenvectors whose eigenvalues are below the line tend to project simulation structure finer than the resolution of the measurement, and thus induce instabilities.

The effectiveness of the regularization is measured with the goodness-of-fit between the $\chi^2(\sin^2\theta_W)$ value of the scan points and the parabolic function. In the basis vector space of the error matrix, the χ^2 of each scan point is $\sum_n(\delta A_{\rm fb})_n^2/(\lambda_n + r_n)$, where the index n runs over all the eigenvector numbers and $\delta A_{\rm fb}$ is the difference between the measured and calculated values of $A_{\rm fb}$. The regularization function shown in Fig. 21 is defined and optimized as follows. The shape of the regularization function is chosen so that it selectively suppresses eigenvectors that project onto noise rather than the uncertainties of the measurement. To identify these eigenvectors, the expansion of the error matrix is truncated one eigenvector at a time. Truncating eigenvectors 14 and 13 from the error matrix significantly improves the goodness-of-fit. There is no further improvement with the truncation

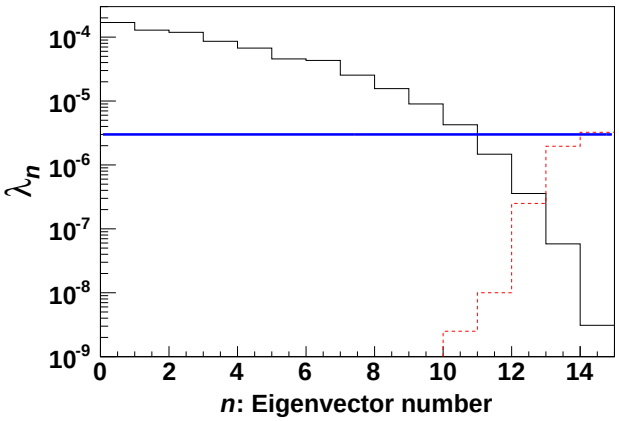

FIG. 21. Eigenvalues of the error matrix (solid histogram), and its regularization terms (dashed histogram). The horizontal line is the square of the statistical uncertainty of the $A_{\rm fb}$ measurement for the mass bin containing the Z peak.

of lower numbered eigenvectors. Consequently, the regularization terms for eigenvectors 13 and 14 are set to values significantly larger than the eigenvalues so that the contributions of their constituents to the χ^2 are negligible. The regularization term for eigenvector 12 is set to a value that is comparable with its companion eigenvalue. For eigenvector numbers 11 and under, the regularization terms are set to zero or values much smaller than the eigenvalues so that their components in the χ^2 are unaffected or negligibly affected by the regularization terms. The optimum normalization level is determined via a scan of level scale-factor values, starting from 0. As the scale-factor value increases, the goodness-of-fit rapidly improves then enters a plateau region without significant improvement and only a degradation of the measurement resolution. The optimum is chosen to be slightly beyond the start of the plateau region, where the $\overline{\sin^2}\theta_W$ parameter is also stable in value.

As a cross check, the extraction of $\sin^2\theta_W$ is performed using only CC or CP events for the measurement of $A_{\rm fb}$ and its error matrix, and the default PDF of NNPDF-3.0 for the calculation of templates. The extracted values using only CC or CP events differ by about 0.6 standard deviations of the statistical uncertainty. Since they are consistent with each other, CC and CP events are hereafter combined. An example template scan extraction of $\sin^2\theta_W$ from the asymmetry of CC and CP events using χ^2 values calculated with the regularized error matrix, and then fit to the parabolic χ^2 function of Eq. (7) is shown in Fig. 22.

The EBA-based tree and POWHEG-BOX NLO calculations of $A_{\rm fb}$ use NNPDF-3.0 PDFs, an ensemble of probability-based PDFs. Such ensembles are random samples drawn from the probability density distribution of PDF parameters constrained by a global fit to prior measurements. Thus, all information within the probability density distribution is utilized. The predicted

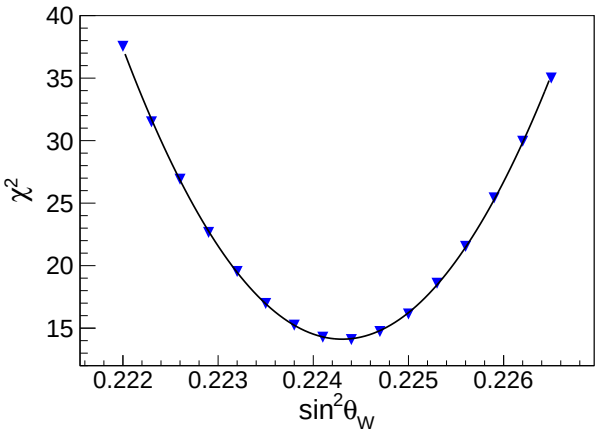

FIG. 22. Values of χ^2 as functions of scan points in the $\sin^2\theta_W$ variable with the parabolic fit overlaid. The triangles are the comparisons of the electron-pair $A_{\rm fb}$ measurement with the POWHEG-BOX NLO calculations. The $A_{\rm fb}$ templates of each scan point are calculated with the default PDF of NNPDF-3.0. The solid curve is the fit of those points to the χ^2 parabolic function.

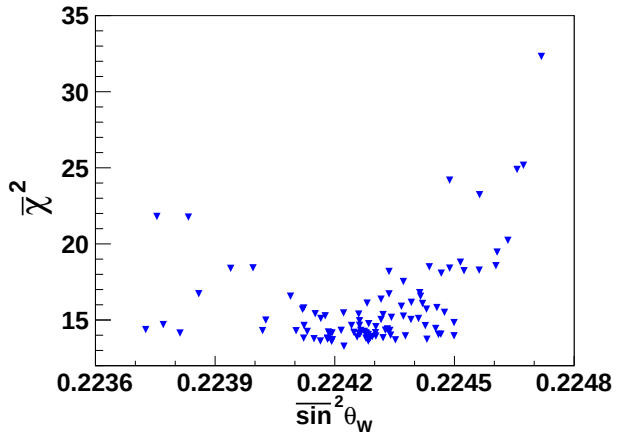

FIG. 23. $\bar{\chi}^2$ versus $\overline{\sin}^2\theta_W$ parameters for the best-fit templates of the POWHEG-BOX NLO calculation for each of the NNPDF-3.0 ensemble PDFs. The $A_{\rm fb}$ measurement with electron pairs covers 15 mass bins.

value of an observable is the convolution of the probability density distribution with the calculation. Consequently, the rms dispersion about the mean is the associated PDF uncertainty [46]. Typically, the PDF ensemble consists of equally likely samples. The NNPDF-3.0 ensemble consists of 100 equally probable samples. New measurements, if compatible with the measurements used to constrain the PDFs, are incorporated into the ensemble without regenerating it. This is accomplished by weighting the ensemble PDFs, numbered 1 to N, with the likelihood of the new measurement being consistent with the calculations:

$$w_k = \frac{\exp(-\frac{1}{2}\chi^2_k)}{\sum_{l=1}^{N}\exp(-\frac{1}{2}\chi^2_l)} \qquad (8)$$

where w_k is the weight for PDF number k, and χ^2_k is the χ^2 between the new measurement and the calculation using that PDF [46, 47]. These weights are denoted as w_k *weights* [46].

The $A_{\rm fb}$ measurement is used simultaneously to extract $\sin^2\theta^{\rm lept}_{\rm eff}$ and to constrain PDFs [48]. Scan templates of $A_{\rm fb}$ are calculated for each ensemble PDF, and its best-fit parameters, $\overline{\sin}^2\theta_W$, $\bar{\chi}^2$ and $\bar{\sigma}$, are derived. Figure 23 shows that the $A_{\rm fb}$ measurement is compatible with those included in the NNPDF-3.0 fits of PDF parameters. The results of the template scans are summarized in Table III. Included in the table for comparison are other measurements of $\sin^2\theta^{\rm lept}_{\rm eff}$; the CDF results are derived from EBA-based QCD templates.

The EBA-based POWHEG-BOX calculations of $A_{\rm fb}$ using the w_k-weighted PDFs give the central value of $\sin^2\theta_W$. The $\bar{\chi}^2$ values listed in Table III indicate that the POWHEG-BOX calculation provides the best description of the $A_{\rm fb}$ measurement. For graphical comparisons of best-fit $A_{\rm fb}$ templates, the difference relative to a reference calculation is used: $A_{\rm fb} - A_{\rm fb}$(PYTHIA) where the reference $A_{\rm fb}$(PYTHIA) is the tuned PYTHIA calculation described in Sec. VI on the signal simulation. Figure 24 shows the difference distributions for the measurement, the POWHEG-BOX calculation, and the RESBOS calculation. The comparison of POWHEG-BOX with NNPDF-3.0 PDFs to RESBOS with CTEQ6.6 PDFs illustrates the nature of $A_{\rm fb}(M)$ as a simultaneous probe of the electroweak-mixing parameter and the PDFs. The NNPDF-3.0 PDFs include collider data from the LHC

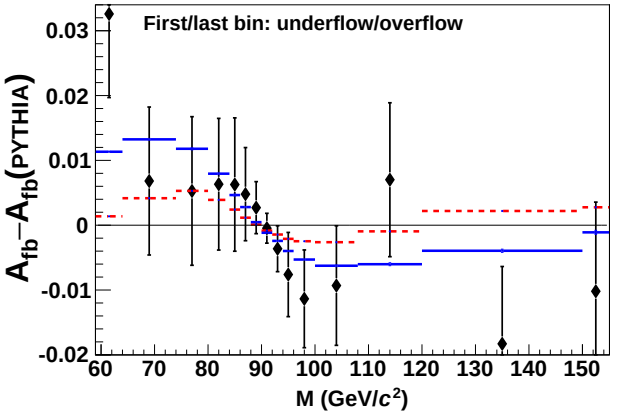

FIG. 24. $A_{\rm fb} - A_{\rm fb}$(PYTHIA) for $|y| < 1.7$. The diamonds represent the measurement using electron pairs, and the uncertainties shown are the bin-by-bin unfolding estimates which are correlated. There are no suppressed measurement values. The solid bars represent the POWHEG-BOX calculation with the default NNPDF-3.0 PDFs. The dashed bars represent the RESBOS calculation with CTEQ6.6 PDFs. Both calculations use $\sin^2\theta_W = 0.2243$. The horizontal line represents the reference PYTHIA calculation which uses CTEQ5L PDFs with $\sin^2\theta^{\rm lept}_{\rm eff} = 0.232$.

TABLE III. Extracted values of $\sin^2\theta^{\rm lept}_{\rm eff}$ and $\sin^2\theta_W$ from the $A_{\rm fb}$ measurement using electron pairs. For the tree and POWHEG-BOX entries, the values are averages over the NNPDF-3.0 ensemble; "weighted" templates denote the w_k-weighted average; and $\delta\sin^2\theta_W$ is the PDF uncertainty. The PYTHIA entry is the value from the scan over non-EBA templates calculated by PYTHIA 6.4 with CTEQ5L PDFs. The uncertainties of the electroweak-mixing parameters are the measurement uncertainties $\bar{\sigma}$. For the $\bar{\chi}^2$ column, the number in parenthesis is the number of mass bins of the $A_{\rm fb}$ measurement.

Template (Measurement)	$\sin^2\theta^{\rm lept}_{\rm eff}$	$\sin^2\theta_W$	$\delta\sin^2\theta_W$	$\bar{\chi}^2$
POWHEG-BOX NLO, default	0.23249 ± 0.00049	0.22429 ± 0.00048	± 0.00020	15.9 (15)
POWHEG-BOX NLO, weighted	0.23248 ± 0.00049	0.22428 ± 0.00048	± 0.00018	15.4 (15)
RESBOS NLO	0.23249 ± 0.00049	0.22429 ± 0.00047	–	21.3 (15)
Tree LO, default	0.23252 ± 0.00049	0.22432 ± 0.00047	± 0.00021	22.4 (15)
Tree LO, weighted	0.23250 ± 0.00049	0.22430 ± 0.00047	± 0.00021	21.5 (15)
PYTHIA	0.23207 ± 0.00046	–	–	24.6 (15)
(CDF 9 fb^{-1} $A_{\rm fb}^{(\mu\mu)}$ [6])	0.2315 ± 0.0010	0.2233 ± 0.0009	–	21.1 (16)
(CDF 2 fb^{-1} $A_4^{(ee)}$ [5])	0.2328 ± 0.0010	0.2246 ± 0.0009	–	–
(LEP-1 and SLD $A_{\rm FB}^{0,{\rm b}}$ [11])	0.23221 ± 0.00029	–	–	–
(SLD $\mathcal{A}_\ell$ [11])	0.23098 ± 0.00026	–	–	–

while the CTEQ6.6 PDFs do not.

X. SYSTEMATIC UNCERTAINTIES

The systematic uncertainties of the results derived from electron pairs contain contributions from both the measurement of $A_{\rm fb}$ and the template predictions of $A_{\rm fb}$ for various input values of $\sin^2\theta_W$. Both the experimental and prediction-related systematic uncertainties are small compared to the experimental statistical uncertainty. The $A_{\rm fb}$ templates of the POWHEG-BOX calculations are used to estimate systematic uncertainties on the $\sin^2\theta_W$ parameter from various sources.

A. Measurement

The measurement uncertainties considered are from the energy scale and resolution, and from the background estimates. The bias-correction uncertainty from the PDFs, expected to be a small secondary effect, is not included. For the propagation of uncertainties to the extracted value of $\sin^2\theta_W$, the default PDF of the NNPDF-3.0 ensemble is used. The total measurement systematic uncertainty is ± 0.00003.

The energy scale and resolution of the simulation and data samples are accurately calibrated (Sec. VII) using electron-pair mass distributions. In conjunction, the mass distributions of the simulation have been tuned to agree with those of the data, and the agreement between them, presented in Figs. 12 and 13 is good. Since the energy scales of the data and simulation are calibrated separately from the underlying-physics scale, the potential effect of an offset between the global scales of the simulation and data is investigated as a systematic uncertainty. The electron-pair mass distributions in the vicinity of the Z-boson mass peak are used to constrain shifts. Scale shifts for the central and plug EM calorimeters are considered separately. The resulting uncertainty from the energy scale is ± 0.00003. The potential effect of the limitations to the energy-resolution model of the simulation is also investigated, and the resulting uncertainty is estimated to be negligible.

For the background systematic uncertainty, the normalization uncertainties of the two largest backgrounds, QCD and $Z \to \tau\tau$, are considered. They amount to about three-quarters of the total background. The uncertainties of their normalization values from the background fits described in Sec. VII C are propagated into uncertainties on $\sin^2\theta_W$. They have a negligible impact on the measurement. For the $Z \to \tau\tau$ background of the CC topology, the difference between the constrained and unconstrained fit normalizations is assigned as a systematic uncertainty. The systematic uncertainty from the background is ± 0.00002.

The bias correction uses the PYTHIA calculation with CTEQ5L PDFs. To evaluate whether a PDF systematic uncertainty is needed, the following bias metric is used: the difference in asymmetries calculated with the measurement rapidity range of $|y| < 1.7$ and with the reduced rapidity range of $|y| < 1.5$. The bias metric calculated with PYTHIA is shown in Fig. 19, along with the PDF uncertainties estimated using the tree-level calculation of $A_{\rm fb}$ with the NNPDF-3.0 ensemble of PDFs. The PDF uncertainties are small when compared to the statistical uncertainties of the bias correction. In addition, the PYTHIA calculation of the bias-metric function is compatible, relative to PDF uncertainties, with the tree-level calculation using NNPDF-3.0 PDFs; the comparison χ^2 has a value of 11 for the 15 mass bins. The PDF uncertainty to the PYTHIA calculation is not included with the measurement because its effects are sufficiently small relative to the statistical uncertainties of the bias correction, and because the prediction includes an uncertainty for PDFs.

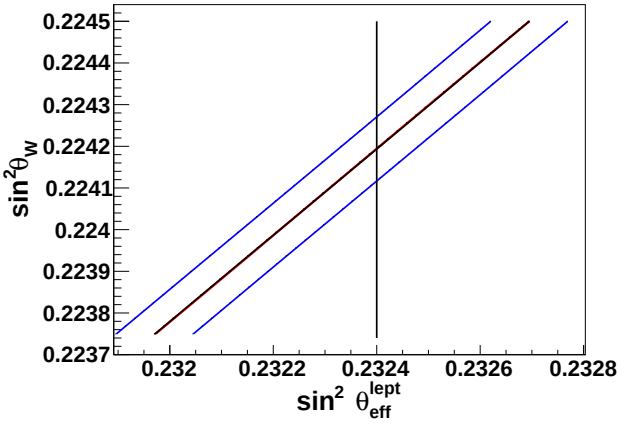

FIG. 25. $\sin^2\theta_W$ versus $\sin^2\theta_{\rm eff}^{\rm lept}$ relationships from ZFITTER calculations. The default calculation is the middle line of the group. The outermost lines are for one standard-deviation shifts to the default value of the top-quark mass parameter (173.2 ± 0.9) [49]; the lower line corresponds to a higher value of the top-quark mass. The lines for one standard-deviation variations of the $\Delta\alpha_{\rm em}^{(5)}(M_Z^2)$ parameter are close to the default calculation and not easily distinguishable. The vertical line, an example reference value for $\sin^2\theta_{\rm eff}^{\rm lept}$, is explained in the text.

B. Predictions

The theoretical uncertainties considered are from the PDFs, higher-order QCD effects, and the ZFITTER calculation. The dominant uncertainty is the PDF uncertainty of ± 0.00018, and it is the w_k-weighted value of $\delta \sin^2\theta_W$ from the POWHEG-BOX NLO entry of Table III. The total prediction uncertainty is ± 0.00020.

The uncertainty of higher-order QCD effects is estimated with the difference between the values of $\sin^2\theta_W$ in Table III extracted with the tree and POWHEG-BOX NLO templates based on the w_k-weighted ensemble of NNPDF-3.0 PDFs. This uncertainty, denoted as the "QCD scale" uncertainty, is ± 0.00002. Although the POWHEG-BOX prediction is a fixed-order NLO QCD calculation at large boson $P_{\rm T}$, it is a resummation calculation in the low-to-moderate $P_{\rm T}$ region. The parton-showering algorithm of PYTHIA incorporates multi-order real emissions of QCD radiation over all regions of the boson $P_{\rm T}$.

The $\sin^2\theta_{\rm eff}^{\rm lept}$ result, because of its direct relationship with $A_{\rm fb}$, is independent of the standard-model based calculations specified in the appendix. However, the choice of input parameter values may affect the fit value of $\sin^2\theta_W$ or M_W. The effect of measurement uncertainties from the top-quark mass m_t and from the contribution of the light quarks to the "running" electromagnetic fine-structure constant at the Z mass $\Delta\alpha_{\rm em}^{(5)}(M_Z^2)$ is investigated using these uncertainties: ± 0.9 GeV/c^2 [49] and ± 0.0001 [50], respectively. Figure 25 shows the relation between $\sin^2\theta_W$ and $\sin^2\theta_{\rm eff}^{\rm lept}$ for the default parameter values, and for one standard-deviation shifts to the default values of the m_t and $\Delta\alpha_{\rm em}^{(5)}(M_Z^2)$ parameters. Offsets from the default parameter curve to the one standard-deviation curves along a reference value for $\sin^2\theta_{\rm eff}^{\rm lept}$ (e.g., the vertical line in Fig. 25) are used as systematic uncertainties to $\sin^2\theta_W$ from the input parameters. The uncertainty to $\sin^2\theta_W$ from $\Delta\alpha_{\rm em}^{(5)}(M_Z^2)$ is negligible, and that from m_t is ± 0.00008. This uncertainty, denoted as the "form factor" uncertainty, is included in systematic uncertainties for $\sin^2\theta_W$ and M_W.

TABLE IV. Summary of the systematic uncertainties on the extraction of the electroweak-mixing parameters $\sin^2\theta_{\rm eff}^{\rm lept}$ and $\sin^2\theta_W$ from the $A_{\rm fb}$ measurement with electron pairs.

Source	$\sin^2\theta_{\rm eff}^{\rm lept}$	$\sin^2\theta_W$
Energy scale	± 0.00003	± 0.00003
Backgrounds	± 0.00002	± 0.00002
NNPDF-3.0 PDF	± 0.00019	± 0.00018
QCD scale	± 0.00002	± 0.00002
Form factor	–	± 0.00008

XI. RESULTS

The values for $\sin^2\theta_{\rm eff}^{\rm lept}$ and $\sin^2\theta_W$ (M_W) extracted from this measurement of $A_{\rm fb}$ are

$$\begin{aligned}\sin^2\theta_{\rm eff}^{\rm lept} &= 0.23248 \pm 0.00049 \pm 0.00019\\ \sin^2\theta_W &= 0.22428 \pm 0.00048 \pm 0.00020\\ M_W \text{ (indirect)} &= 80.313 \pm 0.025 \pm 0.010 \text{ GeV}/c^2\,,\end{aligned}$$

where the first contribution to the uncertainties is statistical and the second is systematic. All systematic uncertainties are combined in quadrature.

A summary of the sources and values of systematic uncertainties is presented in Table IV. The results of this section supersede those derived from the A_4 angular-distribution coefficient of ee-pairs from a sample corresponding to 2.1 fb^{-1} of collisions [5].

XII. CDF RESULT COMBINATION

The measurement of $A_{\rm fb}$ presented in this paper and the previous CDF measurement using Drell-Yan $\mu^+\mu^-$ pairs [6] are used to extract the combined result for the electroweak-mixing parameter. Both measurements are fully corrected and use the full Tevatron Run II data set. Since they are defined for different regions of the lepton-pair rapidity, $|y_{ee}| < 1.7$ and $|y_{\mu\mu}| < 1.0$, each measurement is compared separately to $A_{\rm fb}$ templates calculated with the rapidity restriction of the measurements, and the joint χ^2 is used to extract the combined values for electroweak-mixing parameters $\sin^2\theta_{\rm eff}^{\rm lept}$ and $\sin^2\theta_W$.

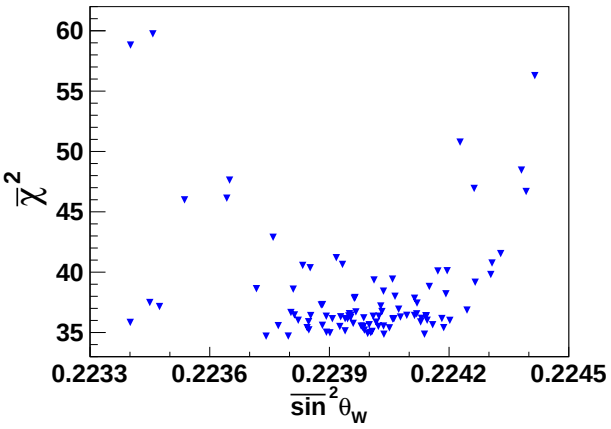

FIG. 26. $\bar{\chi}^2$ versus $\overline{\sin}^2\theta_W$ parameters of the $\mu\mu$- and ee-channel combination. The prediction templates are calculated with POWHEG-BOX NLO and each of the NNPDF-3.0 ensemble PDFs. The $\mu\mu$- and ee-channel $A_{\rm fb}$ measurements contain 16 and 15 mass bins, respectively.

A. Method

The templates for both measurements are calculated using the EBA-based POWHEG-BOX NLO framework and the NNPDF-3.0 PDF ensemble of this analysis. The corresponding tree-level templates are also calculated. The $A_{\rm fb}$ templates for both the $\mu\mu$- and ee-channel measurements are calculated in the same POWHEG-BOX or tree-level computational runs. Thus, they share common events and scan-point values of the $\sin^2\theta_W$ parameter.

The method for the extraction of $\sin^2\theta^{\rm lept}_{\rm eff}$ from each measurement is unaltered. For each of the ensemble PDFs, the parabolic fits to $\chi^2(\sin^2\theta_W)$ shown in Eq. (7) from each measurement are combined to obtain the values of $\overline{\sin}^2\theta_W$, $\bar{\chi}^2$, and $\bar{\sigma}$. Figure 26 shows the $\bar{\chi}^2$ and $\overline{\sin}^2\theta_W$ parameters associated with each ensemble PDF. The corresponding table of fit parameters is provided as supplemental material [51]. The ensemble-averaged values of the individual channels, along with their combination, are shown in Table V. The w_k-weighted averaging method with POWHEG-BOX NLO calculations is selected for the central value of the combination result.

B. Systematic uncertainties

The categories of systematic uncertainties for both the $\mu\mu$- and ee-channel extractions of the electroweak-mixing parameters are the same. Uncertainties associated with the measurements include those on the electroweak-mixing parameter from the backgrounds and the energy scales. Those associated with the predictions include uncertainties from the PDFs and higher-order QCD effects (QCD scale). The numerical values for systematic uncertainties in this section are for the $\sin^2\theta_W$ parameter.

The measurement uncertainties of the $\mu\mu$ and ee channels are uncorrelated, and thus the propagation of their uncertainties to $\sin^2\theta_W$ is uncorrelated. The combined energy-scale and background uncertainties are ±0.00002 and ±0.00003, respectively.

As the prediction uncertainties of both channels are correlated, the corresponding uncertainties of the combination are derived from the fit parameters of the joint χ^2. The uncertainty due to the PDF is ±0.00016, which is the w_k-weighted $\delta\sin^2\theta_W$ value from the POWHEG-BOX NLO entry of Table V. The uncertainty due to the QCD scale is ±0.00007, which is the difference between the w_k-weighted $\sin^2\theta_W$ values of the POWHEG-BOX NLO and Tree entries from Table V.

C. Results

The combination values for $\sin^2\theta^{\rm lept}_{\rm eff}$ and $\sin^2\theta_W$ (M_W) are

$$\begin{aligned}\sin^2\theta^{\rm lept}_{\rm eff} &= 0.23221 \pm 0.00043 \pm 0.00018\\ \sin^2\theta_W &= 0.22400 \pm 0.00041 \pm 0.00019\\ M_W\ \text{(indirect)} &= 80.328 \pm 0.021 \pm 0.010\ \text{GeV}/c^2\,,\end{aligned}$$

where the first contribution to the uncertainties is statistical and the second is systematic. All systematic uncertainties are combined in quadrature, and the sources and values of these uncertainties are summarized in Table VI. The form-factor uncertainty, estimated in Sec. XI, is the uncertainty from the standard-model based calculation specified in the appendix.

The measurements of $\sin^2\theta^{\rm lept}_{\rm eff}$ are compared with previous results from the Tevatron, LHC, LEP-1, and SLC in Fig. 27. The hadron collider results are based on $A_{\rm fb}$ measurements. The LEP-1 and SLD results on $\sin^2\theta^{\rm lept}_{\rm eff}$ are from these asymmetry measurements at the Z pole [11]:

$$\begin{aligned}A^{0,\ell}_{\rm FB} &\to 0.23099 \pm 0.00053\\ \mathcal{A}_\ell(P_\tau) &\to 0.23159 \pm 0.00041\\ \mathcal{A}_\ell(\text{SLD}) &\to 0.23098 \pm 0.00026\\ A^{0,\rm b}_{\rm FB} &\to 0.23221 \pm 0.00029\\ A^{0,\rm c}_{\rm FB} &\to 0.23220 \pm 0.00081\\ Q^{\rm had}_{\rm FB} &\to 0.2324 \pm 0.0012\end{aligned}$$

The $Q^{\rm had}_{\rm FB}$ measurement is based on the hadronic-charge asymmetry from all-hadronic final states.

The W-boson mass inference is compared in Fig. 28 with previous direct and indirect measurements from the Tevatron, NuTeV, LEP-1, SLD, and LEP-2. The direct measurement is from the Tevatron and LEP-2 [52]. The previous indirect measurement from the Tevatron is derived from the CDF measurement of $A_{\rm fb}$ with muon pairs and it uses the same EBA-based method of inference. The indirect measurement of $\sin^2\theta_W$ from LEP-1 and SLD, 0.22332 ± 0.00039, is from the standard-model fit to all Z-pole measurements [11, 12] described in Appendix F

TABLE V. Extracted values of $\sin^2\theta_{\rm eff}^{\rm lept}$ and $\sin^2\theta_W$ after averaging over the NNPDF-3.0 ensembles. The "weighted" templates denote the w_k-weighted ensembles; and $\delta\sin^2\theta_W$ is the PDF uncertainty. The uncertainties of the electroweak-mixing parameters are the measurement uncertainties $\bar{\sigma}$. For the $\bar{\chi}^2$ column, the number in parenthesis is the number of mass bins of the $A_{\rm fb}$ measurement. The ee-channel values are from Table III, and the $\mu\mu$-channel values use the previous CDF measurement of $A_{\rm fb}$ with $\mu^+\mu^-$ pairs [6].

Template	Channel	$\sin^2\theta_{\rm eff}^{\rm lept}$	$\sin^2\theta_W$	$\delta\sin^2\theta_W$	$\bar{\chi}^2$
POWHEG-BOX NLO, default	$\mu\mu$	0.23140 ± 0.00086	0.22316 ± 0.00083	± 0.00029	21.0 (16)
POWHEG-BOX NLO, weighted	$\mu\mu$	0.23141 ± 0.00086	0.22317 ± 0.00083	± 0.00028	20.7 (16)
POWHEG-BOX NLO, default	ee	0.23249 ± 0.00049	0.22429 ± 0.00048	± 0.00020	15.9 (15)
POWHEG-BOX NLO, weighted	ee	0.23248 ± 0.00049	0.22428 ± 0.00048	± 0.00018	15.4 (15)
POWHEG-BOX NLO, default	$ee + \mu\mu$	0.23222 ± 0.00043	0.22401 ± 0.00041	± 0.00021	38.3 (31)
POWHEG-BOX NLO, weighted	$ee + \mu\mu$	0.23221 ± 0.00043	0.22400 ± 0.00041	± 0.00016	35.9 (31)
Tree LO, default	$\mu\mu$	0.23154 ± 0.00085	0.22330 ± 0.00082	± 0.00031	20.9 (16)
Tree LO, weighted	$\mu\mu$	0.23153 ± 0.00085	0.22329 ± 0.00082	± 0.00029	20.5 (16)
Tree LO, default	ee	0.23252 ± 0.00049	0.22432 ± 0.00047	± 0.00021	22.4 (15)
Tree LO, weighted	ee	0.23250 ± 0.00049	0.22430 ± 0.00047	± 0.00021	21.5 (15)
Tree LO, default	$ee + \mu\mu$	0.23228 ± 0.00042	0.22407 ± 0.00041	± 0.00023	44.4 (31)
Tree LO, weighted	$ee + \mu\mu$	0.23215 ± 0.00043	0.22393 ± 0.00041	± 0.00016	37.4 (31)

TABLE VI. Summary of the systematic uncertainties on the $\mu\mu$- and ee-channel combination for the electroweak-mixing parameters $\sin^2\theta_{\rm eff}^{\rm lept}$ and $\sin^2\theta_W$.

Source	$\sin^2\theta_{\rm eff}^{\rm lept}$	$\sin^2\theta_W$
Energy scale	± 0.00002	± 0.00002
Backgrounds	± 0.00003	± 0.00003
NNPDF-3.0 PDF	± 0.00016	± 0.00016
QCD scale	± 0.00006	± 0.00007
Form factor	–	± 0.00008

of Ref. [12]. The following input parameters to ZFITTER, the Higgs-boson mass m_H, the Z-boson mass M_Z, the QCD coupling at the Z pole $\alpha_s(M_Z^2)$, and the QED correction $\Delta\alpha_{\rm em}^{(5)}(M_Z^2)$, are varied simultaneously within the constraints of the LEP-1 and SLD data, while the top-quark mass m_t is constrained to the directly measured value from the Tevatron, 173.2 ± 0.9 GeV/c^2 [49]. The NuTeV value is an inference based on the on-shell $\sin^2\theta_W$ parameter extracted from the measurement of the ratios of the neutral-to-charged current ν and $\bar{\nu}$ cross sections at Fermilab [13].

XIII. SUMMARY

The angular distribution of Drell-Yan lepton pairs provides information on the electroweak-mixing parameter $\sin^2\theta_W$. The electron forward-backward asymmetry in the polar-angle distribution $\cos\vartheta$ is governed by the $A_4\cos\vartheta$ term, whose A_4 coefficient is directly related to the $\sin^2\theta_{\rm eff}^{\rm lept}$ mixing parameter at the lepton vertex, and indirectly to $\sin^2\theta_W$. The effective-leptonic parameter $\sin^2\theta_{\rm eff}^{\rm lept}$ is derived from the measurement of the forward-backward asymmetry $A_{\rm fb}(M)$ based on the entire CDF Run II sample of electron pairs, reconstructed in 9.4 fb^{-1} of integrated luminosity from $p\bar{p}$ collisions at a center-of-momentum energy of 1.96 TeV. Calculations of $A_{\rm fb}(M)$ with different values of the electroweak-mixing parameter are compared with the measurement to determine the value of the parameter that best describes the data. The calculations include QCD radiative corrections and virtual electroweak radiative corrections.

For the ee-channel measurement of $A_{\rm fb}$ presented in this paper, the best-fit values from the comparisons are

$$\begin{aligned}\sin^2\theta_{\rm eff}^{\rm lept} &= 0.23248 \pm 0.00053,\\ \sin^2\theta_W &= 0.22428 \pm 0.00051, \text{ and}\\ M_W(\text{indirect}) &= 80.313 \pm 0.027 \text{ GeV}/c^2\,.\end{aligned}$$

Each uncertainty includes statistical and systematic contributions. The inferred value of $\sin^2\theta_W$ (M_W) is based on the standard-model calculations specified in the appendix. When this measurement of $A_{\rm fb}$ and the previous CDF measurement based on muon pairs [6] are used jointly in fits, the corresponding best-fit values are

$$\begin{aligned}\sin^2\theta_{\rm eff}^{\rm lept} &= 0.23221 \pm 0.00046,\\ \sin^2\theta_W &= 0.22400 \pm 0.00045, \text{ and}\\ M_W(\text{indirect}) &= 80.328 \pm 0.024 \text{ GeV}/c^2\,.\end{aligned}$$

Both results are consistent with LEP-1 and SLD measurements at the Z-boson pole. The value of $\sin^2\theta_{\rm eff}^{\rm lept}$ is also consistent with the previous results from the Tevatron [6, 7].

ACKNOWLEDGMENTS

We thank the Fermilab staff and the technical staffs of the participating institutions for their vital contributions. This work was supported by the U.S. Department of Energy and National Science Foundation; the Italian Istituto Nazionale di Fisica Nucleare; the Ministry of

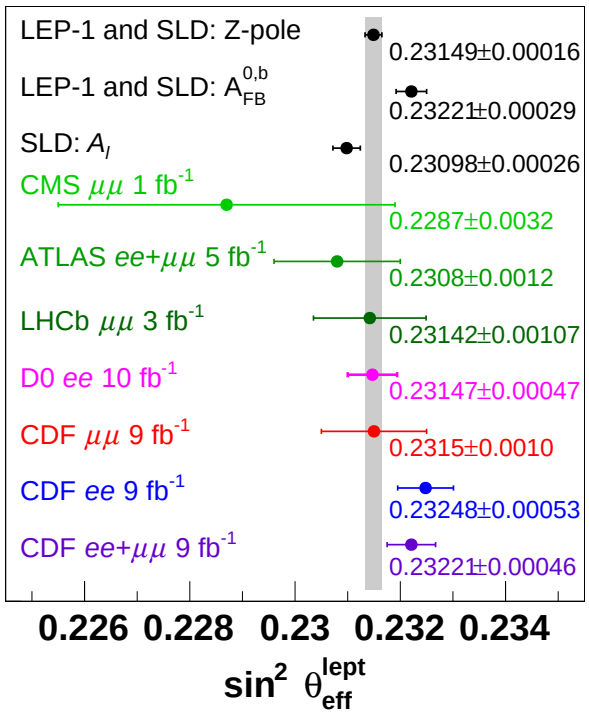

FIG. 27. Comparison of experimental measurements of $\sin^2\theta_{\rm eff}^{\rm lept}$. The horizontal bars represent total uncertainties. The CDF $\mu\mu$-channel, ee-channel, and combination results are denoted as CDF $\mu\mu$ 9 fb^{-1} [6], CDF ee 9 fb^{-1}, and CDF $ee+\mu\mu$ 9 fb^{-1}, respectively. The other measurements are LEP-1 and SLD [11], CMS [9], ATLAS [8], LHCb [10], and D0 [7] The LEP-1 and SLD Z pole result is the combination of their six measurements.

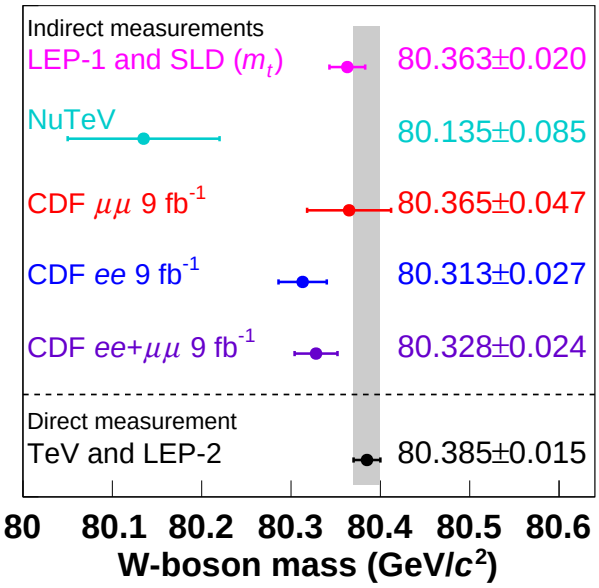

FIG. 28. Comparison of experimental determinations of the W-boson mass. The horizontal bars represent total uncertainties. The CDF $\mu\mu$-channel, ee-channel, and combination results are denoted as CDF $\mu\mu$ 9 fb^{-1} [6], CDF ee 9 fb^{-1}, and CDF $ee+\mu\mu$ 9 fb^{-1}, respectively. The other indirect measurements are from LEP-1 and SLD [11, 12], which include the Tevatron top-quark mass measurement [49], and NuTeV [13]. The direct measurement is from the Tevatron and LEP-2 [52].

Education, Culture, Sports, Science and Technology of Japan; the Natural Sciences and Engineering Research Council of Canada; the National Science Council of the Republic of China; the Swiss National Science Foundation; the A.P. Sloan Foundation; the Bundesministerium für Bildung und Forschung, Germany; the Korean World Class University Program, the National Research Foundation of Korea; the Science and Technology Facilities Council and the Royal Society, United Kingdom; the Russian Foundation for Basic Research; the Ministerio de Ciencia e Innovación, and Programa Consolider-Ingenio 2010, Spain; the Slovak R&D Agency; the Academy of Finland; the Australian Research Council (ARC); and the EU community Marie Curie Fellowship Contract No. 302103.

Appendix: ZFITTER

The input parameters to the ZFITTER radiative-correction calculation are particle masses, the electromagnetic fine-structure constant $\alpha_{\rm em}$, the Fermi constant G_F, the strong-interaction coupling at the Z mass $\alpha_s(M_Z^2)$, and the contribution of the light quarks to the "running" $\alpha_{\rm em}$ at the Z mass $\Delta\alpha^{(5)}_{\rm em}(M_Z^2)$. The scale-dependent couplings are $\alpha_s(M_Z^2) = 0.118 \pm 0.001$ [53] and $\Delta\alpha^{(5)}_{\rm em}(M_Z^2) = 0.0275 \pm 0.0001$ [50]. The mass parameters are $M_Z = 91.1875 \pm 0.0021$ GeV/c^2 [11, 12], $m_t = 173.2 \pm 0.9$ GeV/c^2 (top quark) [49], and $m_H = 125$ GeV/c^2 (Higgs boson). Form factors and the Z-boson total decay-width Γ_Z are calculated. The central values of the parameters provide the context of the ZFITTER standard-model calculations.

ZFITTER uses the on-shell renormalization scheme scheme [3], where particle masses are on-shell and

$$\sin^2\theta_W = 1 - M_W^2/M_Z^2 \qquad \text{(A.1)}$$

holds to all orders of perturbation theory by definition. If both G_F and m_H are specified, $\sin\theta_W$ is not independent, and related to G_F and m_H by standard-model constraints from radiative corrections. To vary the $\sin\theta_W$ (M_W) parameter, the value of G_F is not constrained. The value of the M_W is varied over 80.0–80.5 GeV/c^2, and for each value, ZFITTER calculates G_F and the form factors. Each set of calculations corresponds to a family of physics models with standard-model like couplings where $\sin^2\theta_W$ and the G_F coupling are defined by the M_W parameter. The Higgs-boson mass constraint $m_H = 125$ GeV/c^2 keeps the form factors within the vicinity of standard-model fit values from LEP-1 and SLD [11, 12].

The primary purpose of ZFITTER is to provide tables of form factors for each model. As the form factors are calculated in the massless-fermion approximation, they only depend on the fermion weak isospin and charge, and are distinguished via three indices: e (electron type), u (up-quark type), and d (down-quark type).

For the $ee \to Z \to q\bar{q}$ process, the ZFITTER scattering-amplitude ansatz is

$$\begin{aligned} A_q = \frac{i}{4}\, & \frac{\sqrt{2} G_F M_Z^2}{\hat{s} - (M_Z^2 - i\,\hat{s}\Gamma_Z/M_Z)}\, 4 T_3^e T_3^q\, \rho_{eq} \\ & [\langle\bar{e}|\gamma^\mu(1+\gamma_5)|e\rangle\langle\bar{q}|\gamma_\mu(1+\gamma_5)|q\rangle + \\ & -4|Q_e|\kappa_e \sin^2\theta_W\, \langle\bar{e}|\gamma^\mu|e\rangle\langle\bar{q}|\gamma_\mu(1+\gamma_5)|q\rangle + \\ & -4|Q_q|\kappa_q \sin^2\theta_W\, \langle\bar{e}|\gamma^\mu(1+\gamma_5)|e\rangle\langle\bar{q}|\gamma_\mu|q\rangle + \\ & 16|Q_e Q_q|\kappa_{eq} \sin^4\theta_W \langle\bar{e}|\gamma^\mu|e\rangle\langle\bar{q}|\gamma_\mu|q\rangle]\,, \end{aligned}$$

where $q = u$ or d, the ρ_{eq}, κ_e, κ_q, and κ_{eq} are complex-valued form factors, the bilinear γ matrix terms are covariantly contracted, and $\frac{1}{2}(1+\gamma_5)$ is the left-handed helicity projector in the ZFITTER convention. The κ_e form factors of the A_u and A_d amplitudes are not equivalent; however, at $\hat{s} = M_Z^2$, they are numerically equal.

The ρ_{eq}, κ_e, and κ_q form factors are incorporated into QCD calculations as corrections to the Born-level g_A^f and g_V^f couplings,

$$\begin{aligned} & g_V^f \to \sqrt{\rho_{eq}}\,(T_3^f - 2Q_f\kappa_f\, \sin^2\theta_W) \text{ and} \\ & g_A^f \to \sqrt{\rho_{eq}}\, T_3^f\,, \end{aligned}$$

where $f = e$ or q. The resulting current-current amplitude is similar to A_q, but the $\sin^4\theta_W$ term contains $\kappa_e\kappa_q$. This difference is eliminated by adding the $\sin^4\theta_W$ term of A_q with the replacement of κ_{eq} with $\kappa_{eq} - \kappa_e\kappa_q$ to the current-current amplitude. Implementation details are provided in Ref. [5].

[1] S. D. Drell and T.-M. Yan, Phys. Rev. Lett. **25**, 316 (1970).

[2] K. A. Olive *et al.* (Particle Data Group), Chin. Phys. C **38**, 090001 (2014), and 2015 update.

[3] A. Sirlin, Phys. Rev. D **22**, 971 (1980).

[4] D. Acosta *et al.* (CDF Collaboration), Phys. Rev. D **71**, 052002 (2005).

[5] T. Aaltonen *et al.* (CDF Collaboration), Phys. Rev. D **88**, 072002 (2013); Phys. Rev. D **88**, 079905(E) (2013).

[6] T. Aaltonen *et al.* (CDF Collaboration), Phys. Rev. D **89**, 072005 (2014).

[7] V. M. Abazov *et al.* (D0 Collaboration), Phys. Rev. Lett. **115**, 041801 (2015); Phys. Rev. D **84**, 012007 (2011).

[8] G. Aad *et al.* (ATLAS Collaboration), J. High Energy Phys. **09**, 049 (2015).

[9] S. Chatrchyan *et al.* (CMS Collaboration), Phys. Rev. D **84**, 112002 (2011).

[10] R. Aaij *et al.* (LHCb Collaboration), J. High Energy Phys. **11**, 190 (2015).

[11] The ALEPH, DELPHI, L3, OPAL, SLD Collaborations, the LEP Electroweak Working Group, the SLD Electroweak and Heavy Flavour Groups, Phys. Rept. **427**, 257 (2006).

[12] The ALEPH, DELPHI, L3, OPAL Collaborations, the LEP Electroweak Working Group, Phys. Rept. **532**, 119 (2013).

[13] G. P. Zeller *et al.* (NuTeV Collaboration), Phys. Rev. Lett. **88**, 091802 (2002); Phys. Rev. Lett. **90**, 239902(E) (2003).

[14] A. Aktas *et al.* (H1 Collaboration), Phys. Lett. B **632**, 35 (2006).

[15] J. C. Collins and D. E. Soper, Phys. Rev. D **16**, 2219 (1977).

[16] E. Mirkes, Nucl. Phys. **B387**, 3 (1992); E. Mirkes and J. Ohnemus, Phys. Rev. D **50**, 5692 (1994).

[17] T. Aaltonen *et al.* (CDF Collaboration), Phys. Rev. Lett. **106**, 241801 (2011).

[18] D. Bardin, M. Bilenky, T. Riemann, M. Sachwitz, and H. Vogt, Comput. Phys. Commun. **59**, 303 (1990); D. Bardin, P. Christova, M. Jack, L. Kalinovskaya, A. Olchevski, S. Riemann, and T. Riemann, Comput. Phys. Commun. **133**, 229 (2001); A. Arbuzov, M. Awramik, M. Czakon, A. Freitas, M. Grünewald, K. Monig, S. Riemann, and T. Riemann, Comput. Phys. Commun. **174**, 728 (2006).

[19] P. M. Nadolsky *et al.* (CTEQ Collaboration), Phys. Rev. D **78**, 103004 (2008).

[20] R. D. Ball *et al.* (NNPDF Collaboration), J. High Energy Phys. **04**, 040 (2015); Nucl. Phys. **B867**, 244 (2013); R. D. Ball, V. Bertone, F. Cerutti, L. D. Debbio, S. Forte, A. Guffanti, J. I. Latorre, J. Rojo, and M. Ubiali (NNPDF Collaboration), Nucl. Phys. **B855**, 153 (2012); Nucl. Phys. **B849**, 296 (2011); R. D. Ball, L. D. Debbio, S. Forte, A. Guffanti, J. I. Latorre, J. Rojo, and M. Ubiali (NNPDF Collaboration), Nucl. Phys. **B838**, 136 (2010); R. D. Ball, L. D. Debbio, S. Forte, A. Guffanti, J. I. Latorre, A. Piccione, J. Rojo, and M. Ubiali (NNPDF Collaboration), Nucl. Phys. **B809**, 1 (2009); Nucl. Phys. **B816**, 293 (2009); S. Forte, L. Garrido, J. I. Latorre, and A. Piccione, J. High Energy Phys. **05**, 062 (2002).

[21] G. A. Ladinsky and C.-P. Yuan, Phys. Rev. D **50**, R4239 (1994); C. Balàzs and C.-P. Yuan, Phys. Rev. D **56**, 5558 (1997); F. Landry, R. Brock, P. M. Nadolsky, and C.-P. Yuan, Phys. Rev. D **67**, 073016 (2003); A. Konychev and P. Nadolsky, Phys. Lett. B **633**, 710 (2006).

[22] S. Frixione, P. Nason, and C. Oleari, J. High Energy Phys. **11**, 070 (2007).

[23] S. Alioli, P. Nason, C. Oleari, and E. Re, J. High Energy Phys. **07**, 060 (2008).

[24] J. C. Collins, D. E. Soper, and G. Sterman, Nucl. Phys. **B250**, 199 (1985); J. C. Collins and D. E. Soper, Nucl. Phys. **B193**, 381 (1981); Nucl. Phys. **B197**, 446 (1982); Nucl. Phys. **B213**, 545(E) (1983).

[25] V. V. Sudakov, Sov. Phys. JETP **3**, 65 (1956); Zh. Eksp. Teor. Fiz. **30**, 87 (1956).

[26] T. Sjöstrand, S. Mrenna, and P. Z. Skands, J. High Energy Phys. **05**, 026 (2006).

[27] A. Abulencia *et al.* (CDF Collaboration), J. Phys. G: Nucl. Part. Phys. **34**, 2457 (2007).

[28] T. Affolder *et al.*, Nucl. Instrum. Methods Phys. Res., Sect. A **526**, 249 (2004).

[29] T. Aaltonen *et al.*, Nucl. Instrum. Methods Phys. Res., Sect. A **729**, 153 (2013).

[30] L. Balka *et al.*, Nucl. Instrum. Methods Phys. Res., Sect. A **267**, 272 (1988).

[31] S. Bertolucci *et al.*, Nucl. Instrum. Methods Phys. Res., Sect. A **267**, 301 (1988).

[32] M. Albrow *et al.*, Nucl. Instrum. Methods Phys. Res., Sect. A **480**, 524 (2002).

[33] G. Apollinari *et al.*, Nucl. Instrum. Methods Phys. Res., Sect. A **412**, 515 (1998).

[34] P. de Barbaro, IEEE Trans. Nucl. Sci. **42**, 510 (1995).

[35] T. Sjöstrand, P. Edén, L. Lönnblad, G. Miu, S. Mrenna, and E. Norrbin, Comput. Phys. Commun. **135**, 238 (2001).

[36] H. L. Lai *et al.* (CTEQ Collaboration), Eur. Phys. J. C **12**, 375 (2000).

[37] T. Affolder *et al.* (CDF Collaboration), Phys. Rev. Lett. **84**, 845 (2000).

[38] M. Albrow *et al.* (Tev4LHC QCD Working Group), arXiv:hep-ph/0610012.

[39] G. Grindhammer, M. Rudowicz, and S. Peters, Nucl. Instrum. Methods Phys. Res., Sect. A **290**, 469 (1990).

[40] E. Barberio and Z. Was, Computer Phys. Comm. **79**, 291 (1994); E. Barberio, B. van Eijk, and Z. Was, Computer Phys. Comm. **66**, 115 (1991).

[41] P. Golonka and Z. Was, Eur. Phys. J. C **45**, 97 (2006).

[42] A. Bodek, A. van Dyne, J.-Y. Han, W. Sakumoto, and A. Strelnikov, Eur. Phys. J. C **72**, 2194 (2012).

[43] J. M. Campbell and R. K. Ellis, Phys. Rev. D **60**, 113006 (1999).

[44] D. Acosta *et al.*, Nucl. Instrum. Methods A **494**, 57 (2002).

[45] A. Bodek, Eur. Phys. J. C **67**, 321 (2010).

[46] W. T. Giele and S. Keller, Phys. Rev. D **58**, 094023 (1998).

[47] N. Sato, J. F. Owens, and H. Prosper, Phys. Rev. D **89**, 114020 (2014).

[48] A. Bodek, J.-Y. Han, A. Khukhunaishvili, and W. Sakumoto, Eur. Phys. J. C **76**, 115 (2016).

[49] T. Aaltonen *et al.* (CDF and D0 Collaborations), Phys. Rev. D **86**, 092003 (2012).

[50] F. Jegerlehner, Nuovo Cim. C **034S1**, 31 (2011).

[51] See Supplemental Material at ..URL.. for the table of fit parameter values from the joint χ^2 of comparisons of the individual muon and electron-channel $A_{\rm fb}$ measurements and templates calculated with POWHEG-BOX NLO for each ensemble PDF.

[52] T. Aaltonen *et al.* (CDF and D0 Collaboration), Phys. Rev. D **88**, 052018 (2013).

[53] S. Bethke, Eur. Phys. J. C **64**, 689 (2009).